Coastal climate variability in Northeast Greenland and the role of changing sea ice and fjord ice

Sonika Shahi[1,2], Jakob Abermann[1,2,3], Tiago Silva[1,2], Kirsty Langley[3], Signe Hillerup Larsen[4], Mikhail Mastepanov[5], Wolfgang Schöner[1,2]

[1]Department of Geography and Regional Science, University of Graz, Graz, Austria
[2]Austrian Polar Research Institute, Vienna, Austria
[3]Asiaq-Greenland Survey, Nuuk, Greenland
[4]Geological Survey of Denmark and Greenland, Copenhagen, Denmark
[5]Aarhus University, Aarhus, Denmark

Correspondence to: Sonika Shahi (sonika.shahi@uni-graz.at)

Abstract. The climate in Northeast Greenland is shaped by complex topography and interaction with the cryosphere. To capture this complexity, we use an observational dataset from the Zackenberg region (ZR), (Northeast Greenland) to investigate the local and large-scale factors that determine the slope temperature gradients (STGs) i.e., the temperature gradient along the mountain slope. A synthesis of automated weather stations, reanalysis, and regional climate model were used. Our results show that the surface type and near fjord-ice condition are the dominating factors governing the temporal evolution of the STGs in the ZR. Considering large-scale drivers of STG, we find that shallow, i.e., more positive (inversions) or less negative than the mean condition, STGs are associated with a positive anomaly in geopotential height at 500 hPa and surface pressure over East Greenland. A strong connection between fractional sea-ice cover (SIF) in the Greenland Sea and the terrestrial climate of the ZR is found. Evidently, a positive SIF anomaly coincides with shallow STG since the temperature at the bottom of the valley decreases more than at the top. For example, the mean STG varies by ~4 °C km⁻¹ for a corresponding ~27 % change in SIF. Changing temperatures and precipitation patterns related to SIF variability also affect the surface mass balance (SMB) of the nearby A. P. Olsen Ice Cap. During summer, days with high SIF are associated with a positive SMB anomaly in the ablation area (~16 mm w.e. day⁻¹; indicating less melt) and a negative anomaly in the accumulation area (~-0.3 mm w.e. day⁻¹; indicating less accumulation). The decrease in temperature and snowfall related to the days with high SIF explain this opposite pattern in the ablation and accumulation area.

1 Introduction

Near-surface air temperature is a key indicator of the Earth's climate system and a powerful proxy of the surface energy balance (Ohmura, 2019). Consequently, it is widely used to describe climate change's effects on a variety of environmental processes, particularly regarding the water and energy exchange on a local, regional, and global scale. Additionally, to show changes and sensitivity of various ecosystem components with respect to climate change, air temperature is the key variable. Knowing the spatial distribution of temperature in complex terrain, especially the relationship between temperature and

elevation (i.e., lapse rate), is imperative for accurate melt modeling in glacierized or non-glacierized catchments (Chutko and Lamoureux, 2009; Hulth et al., 2010; Mernild and Liston, 2010). Changes in the physical properties of the atmosphere caused by an increase in greenhouse gases may result in different temperature responses in low-lying compared to

35   mountainous areas (Pepin et al., 2022). Consequently, meteorological station networks with dense temporal and spatial coverage are required to capture the complex temperature patterns attributed to local factors like surface conditions (albedo, roughness, topographic aspect), cold air pooling, and temperature inversions (Rolland, 2003). In addition, knowledge about the atmospheric conditions such as synoptic-scale circulation patterns, wind regimes, and atmospheric moisture is required to explain the observed variations in lapse rates.

40   Trends and variability in surface air temperature are known to be larger in the Arctic region than on the global average, a phenomenon commonly referred to as 'Arctic amplification' (Serreze et al., 2009). This is largely driven by the loss of the sea ice, followed by oceanic heat gain through the ice-albedo feedback, and infrared radiation feedbacks (Serreze et al., 2009; Screen and Simmonds, 2010; Bintanja and Van Der Linden, 2013; Ono et al., 2022). Observational studies of Greenland's temperature time series show a significant coastal warming (Hanna et al., 2021), with pronounced warming on

45   the west coast during the winter (Abermann et al., 2017; Hanna et al., 2012) and weaker but steady warming during the summer months both in West and East Greenland (Abermann et al., 2017; Mernild et al., 2014). During the period 2013– 2017, the rate of temperature increase accelerated especially in the Northeast and North Greenland (Jiang et al., 2020). Moreover, model results suggest that Northeast Greenland is among the most sensitive areas to changing temperature (Schuster et al., 2021; Bintanja and Selten, 2014; Shepherd, 2016). With respect to elevation dependency of temperature

50   trends in the Arctic, Gardner et al. (2009) suggest that under a warming climate near-surface temperature lapse rate decreases.

As near-surface air temperature is influenced by various surface processes (Minder et al., 2010; Pepin and Seidel, 2005), temperature lapse rates are not linear and differ from the vertical environmental lapse rate (ELR) of 6.0–6.5 °C km^{-1}. Thus, one must differentiate between the vertical ELR and the near-surface temperature gradient (Heynen et al., 2016;

55   Thayyen and Dimri, 2018). While the former is mainly controlled by adiabatic effects and stratification, the latter is more strongly influenced by the local surface energy balance (net radiation and turbulent heat fluxes) (Cullen and Marshall, 2011; Marshall et al., 2007; Gao et al., 2012). In this study, we mainly focus on the latter (near-surface temperature gradient) and investigate its variation as well as its drivers.
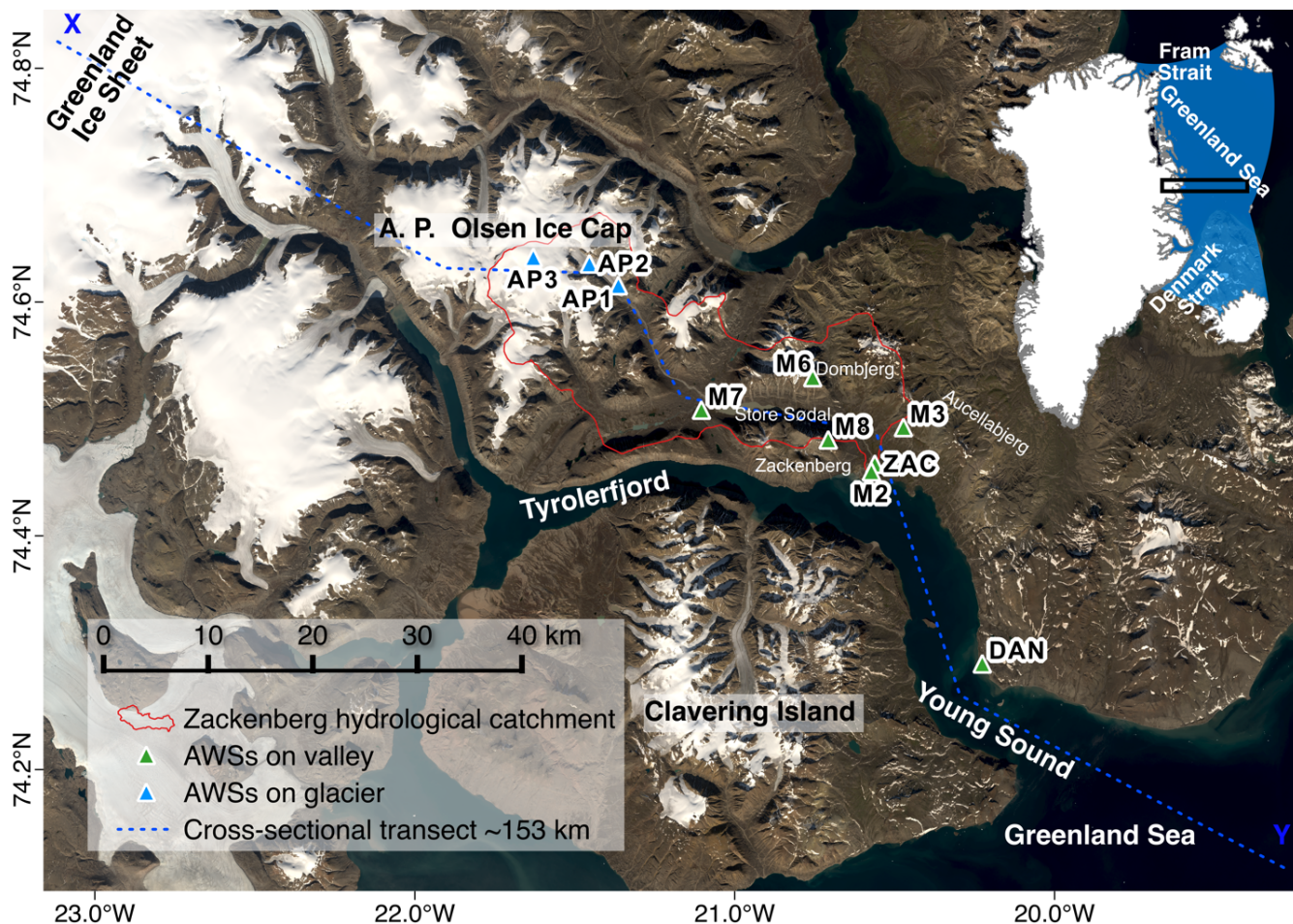
Figure 1. Map of the Zackenberg region (ZR). The location of automated weather stations (AWSs) used in this study on the Zackenberg catchment (red contour) distributed at different elevations and surface types are shown with a triangle; the green triangle indicates AWS on the ice-free surface and blue triangle on the glacier surface. XY (blue) dashed line represents the cross-sectional transect of ~153 km in length passing from the Greenland Ice Sheet (GrIS) (from the west) towards the Greenland Sea (to east) along the ZR and Young Sound. The inset image shows the location of the ZR in Greenland (within a black rectangle) and the Greenland Sea (~1.2×10⁶ km², blue shade) located at the east of Greenland and west of the Svalbard archipelago. The black rectangle indicates an area that is zoomed-in for the purpose of studying sea-ice-related terrestrial local-scale anomalies in the follow-up figures. The (meridional) length of the black rectangle represents the distance from the GrIS (to the west) to the average sea-ice extent for the summer season (to the east), while its (zonal) width covers the ZR. The Greenland Sea is defined by the International Hydrographic Organization (available online at http://www.marineregions.org/.). The base image is Landsat 8 imagery retrieved on 2017-08-24

To study and understand climate variability in the coastal area of Greenland, either dense meteorological station networks or high-resolution atmospheric model simulations are needed. We use both datasets; thus, we can utilize climate information in the large domain. For Greenland, such a dense station network is only available for the Zackenberg region (ZR) (Northeast Greenland), serving as a "research laboratory", as part of the Greenland Ecosystem Monitoring (GEM) program (https://g-e-m.dk) (Fig. 1; see Sect. 2.2). The unusually high spatial resolution of observations in the ZR provides an opportunity to combine data sets to gain a better understanding of how an arctic environment responds to a changing climate

and the related feedback mechanisms. Abermann et al. (2017) found weaker but statistically significant climate trends in Zackenberg compared to overall Greenland climate trends. They suggested that changes in this region's ecosystem due to climate drivers might thus be weaker than changes in more sensitive areas of Greenland.

80   Previous studies showed a positive correlation between the temperature in Greenland and persistent, strong 500 hPa anticyclone over Greenland, which is commonly quantified through the Greenland Blocking Index (GBI) (Hanna et al., 2021; Jiang et al., 2020; Ballinger et al., 2018a, b). Large positive GBI values are often connected with atmospheric blocking events (Hanna et al., 2016). During the blocking event, the polar jet streams develop nearly stationary meanders and trap a warm air mass equatorward of an anticyclonic ridge (Sirpa et al., 2011; Hanna et al., 2015). Atmospheric blocking,

85 depending on the location of the block, can advect warm air across Greenland (especially over western Greenland) (Fettweis et al., 2011, 2013; Hanna et al., 2016, 2014) or stimulate adiabatic descent (or large-scale subsidence) and warms the low-tropospheric air (Ding et al., 2017; Hofer et al., 2017). Since the GBI merely measures the average geopotential height at 500 hPa pressure level (Z500) over Greenland, not the types or locations of the blocking anticyclones (Preece et al., 2022), it can affect regional climates differently. For instance, Preece et al. (2022) found cyclonic wave breaking patterns (a type of

90 blocking that occurs when the anticyclone approaches Greenland from the east along the poleward flank of a cutoff low) produce more melt in Northeast Greenland. This underscores the need to analyze the potential connection between the atmospheric circulation and climate variability in topographically complex regions like ZR, which to our knowledge has not been undertaken in the past.

    Fractional sea-ice cover (SIF) is known to be a relevant driver of the atmospheric state in nearby regions in the Arctic

95 (Stroeve et al., 2017, 2014; Müller et al., 2021; Schuster et al., 2021; Stranne et al., 2021; Isaksen et al., 2022). This is relevant for Zackenberg as it is situated inside a protected fjord system close to the coast (Fig. 1). Yet it exhibits a continental climate with very cold winters and low precipitation due to a wide belt of SIF. Local climate change in Zackenberg will therefore be determined by the SIF variability (Stendel et al., 2008). Variations in sea-ice export through the Greenland Sea (GrSea), as well as the North Atlantic Oscillation (NAO), have an important impact on the spatiotemporal

100 variability of the climate in the ZR, especially the precipitation and surface temperature. Reduction in SIF leads to an increase in precipitation and temperature (Hinkler, 2005; Hansen et al., 2008). However, the direct observational linkages between the SIF variability and terrestrial local temperature gradients along the mountain slope in the ZR have not been analyzed.

    In summary, a recent increase in research into fundamental processes in Northeast Greenland has arisen from the

105 region's sensitivity to global climate change. Despite this, there exists a distinct knowledge gap, especially regarding the consistency of the observed spatial and temporal variability of temperature gradients in the orographically complex terrain, for which the ZR is a useful showcase. To close this gap, this study aims to better understand the coastal near climate variability in Zackenberg, mainly looking at 2 m air temperature (T_{2m}), and the relevant driving mechanisms using a dense network of automated weather stations (AWSs) and combining data from atmospheric reanalysis and a regional climate

110 model. To achieve this general aim, the paper has the following objectives: (1) to estimate the role of surface conditions,

general atmospheric circulation, and weather conditions in controlling vertical differences in the change of air temperatures, and hence the slope temperature gradient (STG; see Sect. 2.8); and (2) to diagnose the physical causes of STG variability due to SIF change. Finally, we discuss the implication of STG and SIF variability on the surface mass balance (SMB) of a local ice cap, A. P. Olsen Ice Cap (APO), (Fig. 1). By doing so, the present study examines the statistical relationship between STG, SIF, and other atmospheric variables. Through this, we intend to gain insights into the physical mechanisms driving the established connections.

2   Data and methods

2.1   Physical setting/site description

The long-term spatiotemporal air temperature monitoring program at the ZR (74.5° N, 20.5° W) made this region a good choice for our study. To investigate the relevant drivers of the STG variability in the ZR, areas toward the GrSea as well as towards the Greenland Ice Sheet (GrIS) are included as regions of interest (Fig. 1). The ZR is located in Northeast Greenland, midway between the outer coast (~40 km to the west) and the GrIS (~70 km to the east). The area shows a high degree of complexity with respect to mountain orography (reaching up to 1450 m a.s.l.) and a wide valley reaching sea level and joining fjords (Young Sound and Tyrolerfjord). A network of AWSs measuring meteorological variables is installed within the 2–3 km wide valley. The location of the AWSs used is shown in Fig. 1. The longest-running AWS is ZAC, which was established in 1995 (Fig. 1). Based on the data from ZAC, the monthly average T_{2m} is highest in July (+6 °C) and lowest in February (-20 °C), based on the period 1996–2019. The mean total annual precipitation is 204 mm for 1996–2020. The area has a polar night for ~89 days (7 November–3 February) and a polar day for ~106 days (30 April–13 August) (Hansen et al., 2008). The Zackenberg River catchment covers 514 km^2, 20 % of which is glacierized (Meltofte and Rasch, 2008).

APO (74.6° N, 21.5° W) is the largest ice cap in the Zackenberg River catchment, of which the southeast-flowing outlet glacier is a key contributor to the meltwater (Mernild et al., 2008), (Fig. 1). The glacier is situated around 35 km northwest of ZAC, disconnected from the GrIS. It is also instrumented with AWSs as a part of GEM (Fig. 1).

Air temperature inversions, atmospheric configurations where temperature increases with height, occur regularly in the ZR (Hansen et al., 2008). For the period 2004–2018, in between ZAC and M3 (where M3 is representative of the area above the inversion layer), inversions are frequent (70–75 %) during winter, whereas during summer the inversion frequency decreases (27–58 %). This local-scale seasonal inversion pattern is consistent with a recent reanalysis-based study for the entire Greenland (Shahi et al., 2020).

2.2   Automated weather stations data

140

Table 1. Overview of all automated weather stations used in this study covering different surface types

Monitoring programme/ institution	Station	Surface type	Latitude (° N)	Longitude (° W)	Elevation (m a.s.l.)	Operation period
ClimateBasis	ZAC		74.47	20.55	43	1995–
GeoBasis	M2	Tundra	74.46	20.56	17	2003–
	M3		74.50	20.46	420	2003–
	M6	Rocks and boulders	74.54	20.74	1282	2006–2010
	M7		74.51	21.10	145	2008–
	M8		74.49	20.70	1144	2013–
GlacioBasis	AP1	Ice/Snow	74.62	21.37	660	2008–
	AP2		74.64	21.47	880	2008–
	AP3		74.64	21.65	1475	2009–
DMI	DAN	Tundra	74.30	20.21	44	2009–2016

This study uses the meteorological data measured by several AWSs operating under GEM. It is a long-term research

145 program on climate change effects and ecosystem interaction initiated in 1995 and has been collecting long-term interdisciplinary environmental datasets at Zackenberg (Meltofte and Thing, 1996; Elberling et al., 2008; Olesen et al., 2010). We use meteorological data from three sub-programs: ClimateBasis (ZAC), (GEM, 2020a), GeoBasis (M2, M3, M6, M7, and M8), (GEM, 2020b, c, d, e, f), and GlacioBasis (AP1, AP2, and AP3), (GEM, 2020g, i, h), (Fig. 1 and Table 1). These AWSs are distributed at different elevations and over different surface types: while three AWSs are located on the

150 APO, six AWSs are over gravel or tundra surfaces in the ZR (Table 1). Additionally, we use meteorological data from station Daneborg (DAN), located 23 km east of ZAC near the outer coast (Cappelen et al., 2001), operated by the Danish Meteorological Institute (DMI), (Fig. 1 and Table 1). This provides excellent spatial and vertical coverage for the investigation of inversion layer formation and destruction processes that occur near the surface. The dataset from the monitoring programs is comprehensively described in Jensen et al. (2014) and as metadata accompanied by the GEM

155 database. All stations are equipped with sensors for T_{2m}, relative humidity, wind speed (U) at 2m (U_{2m}) and direction, and the surface pressure (P_{surf}). A smaller set of stations is also equipped with radiometers and snow depth sensors (Table S1). These stations have a variety of exposition relative to the surrounding terrain and many of the low elevation valley stations are likely to at least occasionally reside in localized cold air pools.
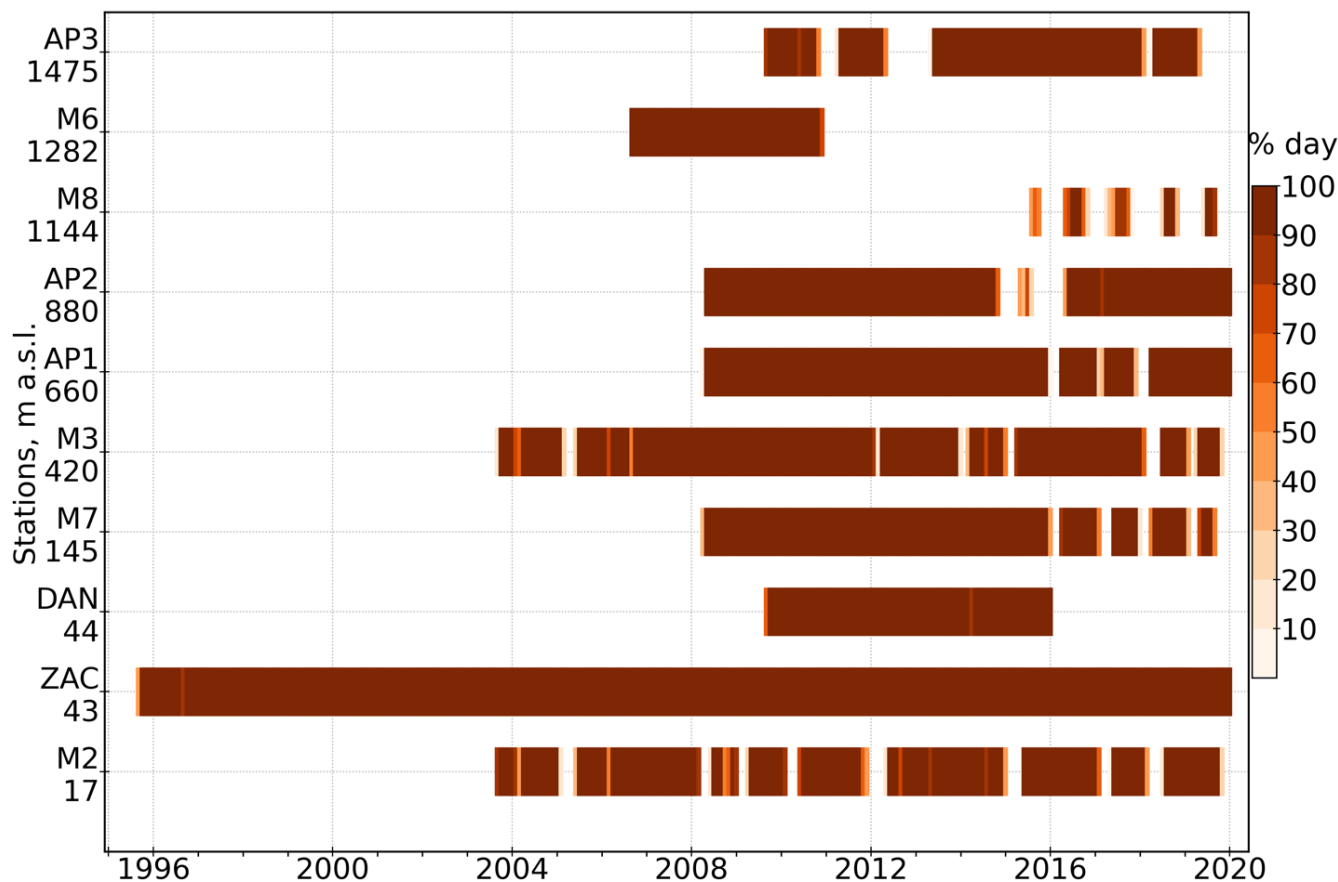
Figure 2. Temporal coverage of all AWSs located on the ZR and on the APO and the elevation of each station in meters above mean sea level (m a.s.l.). The color bar indicates the percentage of days with air temperature data during a respective month for each AWS after screening

The following quality control procedures were applied to the meteorological data: first, we manually corrected the raw data by removing physically unrealistic outliers by visualization of the time series. Second, we calculated the daily means provided that at least 80 % of the hourly measurements were recorded (Abermann et al., 2017). Similarly, monthly means are calculated if more than 80 % of the daily means exist. Figure 2 shows the percentage of days with T_{2m} data during a respective month for each AWS after screening.

The relative humidity was corrected for unrealistic measurements below 0 °C to values for ice using the method proposed by Anderson (1994). As a result, the relative humidity with respect to liquid water below 0 ºC measurements was multiplied by the ratio of the saturation pressure of water and ice.

2.3 Derived variables

The 2-m specific humidity (q_{2m}) was calculated from relative humidity and saturation specific humidity. Firstly, we calculated the saturation vapor pressure over ice and water following Goff & Gratch (1946). Secondly, using the saturation

vapor pressure values, saturation specific humidity was calculated (Fausto et al., 2021). Finally, the specific humidity was estimated using relative humidity and saturation specific humidity.

For all the sites, we estimated the longwave-equivalent cloud cover fraction based on the strong relationship between T_{2m} and the incoming longwave radiation (LWR_{in}) (Van As, 2011). For this, we used the approach developed by Swinbank (1963) to calculate a theoretical LWR_{in} corresponding to both clear-sky conditions as a function of T_{2m}, and overcast conditions assuming blackbody radiation. The cloud cover fraction (CCF) is then calculated by linear interpolation of the LWR_{in} between the clear-sky and overcast estimates. Essentially, the CCF computed with observed variables is closely associated with sky emissivity, rather than the physical fraction of the sky covered by clouds (Djoumna et al., 2021). See Van As (2011) for more details on the CCF estimation.

2.4   Fjord-ice conditions

We use information about the fjord-ice formation and break-up period in the outer Young Sound (Fig. 1) from the MarineBasis sub-program of GEM (GEM, 2020j). The dates for onset and breakup of fjord-ice in outer Young Sound are based on satellite images and local cameras.

2.5   Event-based vertical profiling with unmanned aerial vehicle platform and iMET-XQ2 sensor

An optimal combination of unmanned aerial vehicles (UAVs) and small meteorological sensors provides the potential for measurements of atmospheric variables in a high spatio-temporal resolution (Kimball et al., 2020). Since UAV provides a dynamic and flexible platform for meteorological data acquisition, it has been used widely in exploring atmospheric boundary layer conditions and features, such as inversions and vertical profiles (Kimball et al., 2020; de Boer et al., 2020; Hemingway et al., 2017).

In the summers of 2017 and 2018, field campaigns were carried out in order to measure high-resolution vertical air temperature profiles close to ZAC using the International Met System iMET-XQ2 (iMet-XQ2 Second-Generation Atmospheric Sensor for UAV Deployment, 2021) sensor mounted onto a DJI MAVIC Pro multirotor aircraft. Table S2 shows the specifications of the temperature sensor and GPS used for the measurements. The iMET-XQ2 is a self-contained sensor package designed for UAVs to measure atmospheric temperature, pressure, and relative humidity. It is also equipped with a built-in GPS and an internal data logger along with a rechargeable battery.
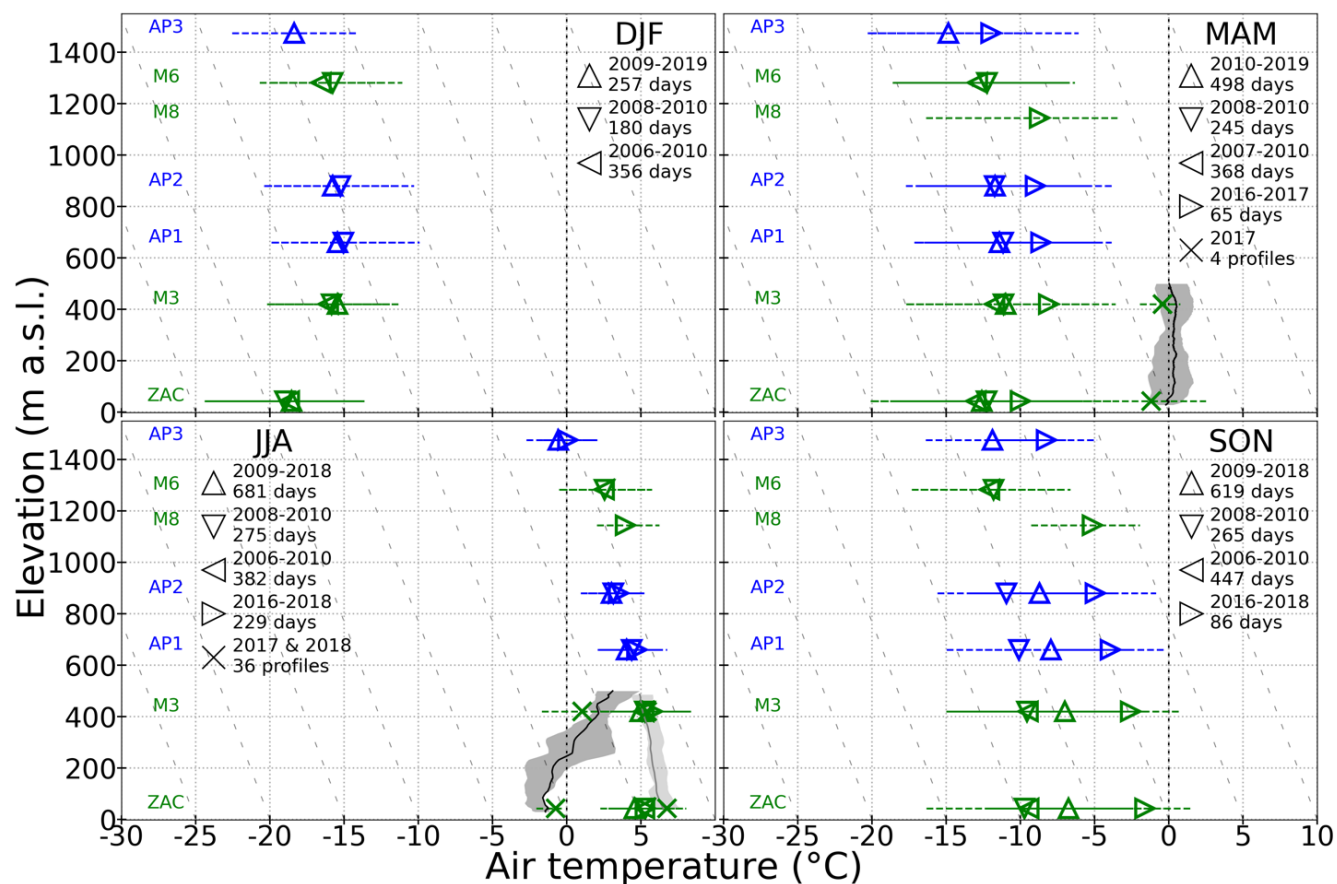
Figure 3. Mean air temperature measurements from AWSs and UAV against the elevation. Each marker (except for the cross) represents the daily mean temperature of a station for temporally overlapping periods, as shown in the legend, with other AWSs measurements for each season. The 25th and 75th percentiles of air temperature are indicated by the dashed horizontal line passing across the marker. Blue and green colors represent stations on ice and ice-free surface, respectively. The mean vertical temperature profile measurements from UAV taken in 2017 (black line) and 2018 (solid grey line) are shown (in MAM and JJA panel) after applying Savitzky Golay low-pass filter to remove the high-frequency fluctuation of air temperature due to the high temporal resolution of UAV. The shaded area around the line represents the 25th and 75th percentiles of the temperature at the given elevation from all vertical profiles. The cross marker represents the sub-daily temperature of a station temporally overlapping with the UAV flight period. In each panel the mean environmental lapse rate (dashed grey line) of 6.5 ºC km^{-1} is plotted for reference

In total, we used 40 temperature profiles (16 from 2017; 24 from 2018), (Figs. 3 and S1). Since the vertical resolution of the temperature profiles measured by UAV is high, we first averaged the data over the height intervals of 1 m, and then, smoothed it at 25-m interval using the Savtizky Golay low-pass filter (Savitzky and Golay, 1964), considering the vertical accuracy of GPS (12 m; Table S2). Air temperature measurements from the UAV at the same time and height as ZAC and M3 were extracted for comparison (Figs. 3 and S1).

2.6   ERA5

We use the fifth-generation atmospheric reanalysis ERA5, a product of the European Centre for Medium-Range Weather Forecasts (ECWWF) from 1979 onwards (Hersbach et al., 2020). In particular, we use the daily mean upper-air variable such as Z500 and P_{surf} (Hersbach et al., 2018b, a). Additionally, the daily SIF from ERA5, interpolated and prescribed to the Regional Atmospheric Climate Model (RACMO) grid at 5.5 km (detailed in Sect. 2.7), was used.

ERA5 has a horizontal resolution of approximately ~0.25° (~15 km over the study region), with 137 model levels, from the surface up to 0.01 hPa (~80 km). It shows many improvements compared to its predecessor (ERA-15, ERA-40, and most recently ERA-Interim) in converting the model values to observation equivalents, and in the processing of observations in the Integrated Forecasting System (IFS Cy41r2 4D-Var), (Graham et al., 2019; Delhasse et al., 2020). In addition, various newly reprocessed datasets have been assimilated and show consistent sea surface temperature and sea ice (Hersbach et al., 2019).

The SIF data are derived from satellite passive microwave brightness temperatures from the series of SMMR, SSM/I, and SSMIS sensors and are prescribed in ERA5 (along with sea surface temperatures) to provide sea surface boundary conditions for the ERA5 atmospheric model. The following processing steps are considered when these products are ingested into ERA5: (1) removal of <15 % SIF; (2) interpolation to the ERA5 model grid; (3) prescribing ice-free conditions for sea surface temperature >3 °C (C3S, 2019).

2.7   The Regional Atmospheric Climate Model

We use the polar version of the Regional Atmospheric Climate Model (RACMO), version 2.3p2, with a horizontal resolution of 5.5 km for the period 1990–2020 (Van Meijgaard et al., 2008; Noël et al., 2015). The polar version of RACMO was developed by the Institute for Marine and Atmospheric Research (IMAU), Utrecht University, with the primary aim to represent the evolution of SMB of glaciated regions such as Greenland (Noël et al., 2015). RACMO encompasses the dynamical core of the High Resolution Limited Area Model (HIRLAM) and the atmospheric physics module from the ECMWF IFS (Noël et al., 2015). At the lateral atmospheric boundaries, the model is forced by ERA5 (1990–2020) at a 6-hourly time interval within 24-grid cells wide relaxation zone (Noël et al., 2019). At each of the 40 vertical atmospheric model levels, the following atmospheric forcing is prescribed: temperature, specific humidity, pressure, wind speed, and direction. Furthermore, the daily SIF and sea surface temperature are not generated by RACMO itself but are prescribed from ERA5 (1990–2020), after being interpolated onto the RACMO model grid (5.5 km). For a detailed model description, we refer to Noël et al. (2019).

We use the daily variables of air temperature and specific humidity at 1000 hPa, 925 hPa, 850 hPa, 700 hPa, and 500 hPa pressure levels from RACMO. The daily near-surface variables used include T_{2m}, q_{2m}, P_{surf}, U at 10 m (U_{10m}), and vertically integrated cloud content, i.e., ice (IWP) and liquid (LWP) water paths. The daily SIF interpolated to the RACMO grid is also used in this study.

Noël et al. (2019) evaluated the simulated GrIS climate using in situ measurements; they found that RACMO closely represents the near-surface climate ($0.73 < R^2 < 0.98$) at 37 AWSs. However, the near-surface climate evaluation done by Noël et al. (2019) does not cover stations on the ice-free surface, since RACMO was developed for studies focusing on the GrIS. Since most of the AWSs in our study domain are on the orographically complex ice-free surface (Fig. 1), a thorough evaluation of RACMO is a crucial prerequisite.

For model evaluation, we used thoroughly quality-controlled daily meteorological data as described in Sects. 2.2 and 2.3, and the temporally overlapping RACMO subsampled grid cell nearest to the observation site (Fig. S2 and Table S3). Unlike Noël et al. (2019), we did not use the elevation criteria (<100 m) to select the nearest grid cell. Table S3 shows that RACMO bias varies amongst variables and stations. The modeled and measured T_{2m} and q_{2m} agrees well for all stations in all seasons ($0.5 < R^2 < 0.9$). However, biases are smaller for stations on the ice compared to gravel or tundra surfaces. A bias for P_{surf} is found, which evidently is the result of the elevation difference between the station and the model (Noël et al., 2019). Discrepancies in modeled U_{10m} and observed U_{2m} can be partly attributed to sensor uncertainty, modeled P_{surf}, and the height at which U is measured (2 m) and modeled (10 m). Despite the elevation and pressure bias, RACMO can resolve the local wind direction (i.e., sea breeze; Fig. S3) in the ZR, especially during summer. Overall, discrepancies exist between model and observations, however, RACMO represents the seasonal pattern appropriately, which is the basis for composite analysis (see Sect. 2.9).

We also used a 1-km SMB product, statistically downscaled from the output of the regional atmospheric climate model RACMO 2.3 (resolution of 11 km) (Noël et al., 2017). Noël et al. (2017) evaluated the 1-km SMB product against observed data for the APO and found close agreement between the downscaled SMB and observations ($R^2=\sim0.7$). Additionally, 1-km air temperature and snowfall data for the APO are also used.

2.8 Slope temperature gradient

Following Glickman (2000), the lapse rate is the change of an atmospheric variable with height, the variable being temperature, unless otherwise specified. On average, temperature decreases with elevation above sea level to the tropopause at the rate of ~6.5 ºC km^{-1}—commonly referred to as the vertical environmental lapse rate. However, the temperature gradient along the mountain slopes significantly varies from the environmental lapse rate (Heynen et al., 2016; Thayyen and Dimri, 2018). This is due to the fact that orographic effects and surface processes strongly control the temperature regime, and hence, alter the near-surface boundary layer (Ayala et al., 2016). In this study, the temperature gradient along the mountain slope is termed slope temperature gradient (STG). This temporally and spatially varying STG (°C km^{-1}) is calculated as,

$$STG_{US-LS} = \frac{T_{US} - T_{LS}}{z_{US} - z_{LS}}$$

where T and z are mean temperatures and elevations, respectively, of lower station (LS) and upper station (US). The station pairs used to calculate STG are indicated as a subscript unless otherwise stated; for instance, the $STG_{M3\text{-}ZAC}$ denotes the STG between M3 (US) and ZAC (LS).

280   Reference to an increase or decrease in the lapse rate terminology can lead to ambiguity. To avoid confusion, we follow the terminology proposed by Pepin and Losleben (2002), where a 'steep' STG is a rapid decrease of temperature with elevation, and a 'shallow' STG is a less negative or positive STG (i.e., temperature inversions). Additionally, 'strong' and 'weak' inversions refer to more and less positive STG, respectively.

2.9   Composite analysis technique

285   **2.9.1   Based on the slope temperature gradient**

We employed a composite analysis technique to scrutinize the link between STG, and near-surface and synoptic-scale climate variables to avoid the assumptions corresponding to linear correlation analysis between these variables (Schweiger et al., 2008; Laken and Čalogović, 2013). This technique highlights the low-amplitude signal within data which otherwise would be muted due to background variability (Laken and Čalogović, 2013). The subset of data is selected based on
290   objective criteria e.g., days with shallow STG, and then averaged (Forbush et al., 1983). Consequently, low-amplitude signals are isolated and become visible due to the reduction in the stochastic background variability (Laken and Čalogović, 2013). The resulting composite anomaly can emphasize the potential relationship between atmospheric phenomena and the variables used for the composite segregation.

The composites of atmospheric and surface variables were computed corresponding to days with high and low STG in
295   Zackenberg. Let $STG_{US-LS}(d_{all})$ be the daily STG between a pair of stations for the given season with d_{all} number of days; STG_μ and STG_σ are the temporal mean and standard deviation, respectively, of $STG_{US-LS}(d_{all})$. Based on that, we classified days as high and low STG days. For high STG days, let d_+ be the selected days in the given season that fulfill $STG_{US-LS}(d_+) > STG_\mu + 0.5\ STG_\sigma$. Likewise, for low STG days, let d_- be the selected days in the given season that fulfill $STG_{US-LS}(d_-) < STG_\mu - 0.5\ STG_\sigma$. Finally, we computed high (V_+) and low (V_-) composite means for the variable V (e.g.,
300   SIF) at geographic location (lon, lat) as,

$$V_+(lon, lat) = \frac{1}{N_+} \sum_{i_+} V(lon, lat, d_+)$$

$$V_-(lon, lat) = \frac{1}{N_-} \sum_{i_-} V(lon, lat, d_-)$$

where N_+ and N_- are the total number of high and low STG days, respectively. Since the selection of composites is based on a unidimensional variation of STG (i.e., it only varies temporally), all grid cells of the composited variables (e.g.,
305   SIF, which varies in space and time) contain means over the same subset of days (i.e., d_+ and d_- are same for all grid cells).

To ensure the robustness of the applied method and reproducibility of the results, we used several other criteria and cross-checked the computed composites. First, we used STG calculated from various pairs of stations to compute

corresponding composited variables following the aforementioned criterion. Additionally, we used criteria based on the 25th and 75th percentiles of the STG distribution in order to isolate high and low STG days, respectively. This was done to

310   objectively evaluate the potential of the applied threshold (i.e., $STG_\mu \pm 0.5\,STG_\sigma$) to get the low amplitude signal on two extreme sides of the data spectrum (~66 % of data). Furthermore, the representativeness of the sample size was tested by using several sample sizes of STG based on all available days, exclusively inversions (positive shallow STG) and non-inversions (steep STG) days, and compare the anomaly patterns of the composited variable. Also, STGs, calculated from different pairs of temporally overlapping stations, were used to compute the composites, to check the consistency of the

315   results produced by different station pairs for the same sample size. Since all the aforementioned criteria show similar anomaly patterns (see Sect. 3.2), all results based on $STG_\mu \pm 0.5\,STG_\sigma$ and for all available days for STG variations will be shown.

2.9.2 Based on sea ice

To investigate the possible link between SIF, near-surface and upper-air atmospheric conditions, and consequently STG, we

320   applied the following criteria in defining high and low SIF days. The criterion is similar to the one used for STG, however since SIF is typically not normally distributed, 95th and 5th percentiles were used to discern high and low SIF days.

Let $SIF(d_{all})$ be the daily SIF for the given season with d_{all} number of days; SIF_{95th} and SIF_{5th} are the 95th and 5th percentiles, respectively, of $SIF(d_{all})$. High and low SIF days are the days when $SIF(d_+) > SIF_{95th}$, and $SIF(d_-) < SIF_{5th}$, respectively. When SIF_{5th} is equal to zero, all days with zero SIF are considered low SIF days.

325   Two sets of composites were calculated based on SIF: the first set of composited variables is based on local information of SIF from the same grid cell, and thus, includes regions only covered by sea ice. This approach increases the probability of identifying signals in atmospheric phenomena due to local changes in SIF. The second set of composite variables is based on a daily time series (1996–2020) of zonally (overall grid cells) averaged (median) SIF over the GrSea (Figs. 1 and S4). Thus, the corresponding composited variables include inland regions beyond sea-ice coverage. The first set of composited

330   variables shows the spatial heterogeneity of composite anomalies due to SIF variability within the same grid cell. Since these composites are based on SIF from the same grid cell, bordering grid cells do not essentially contain the average over the same subset of days (i.e., d_+ and d_- might not be the same for all grid cells). In contrast, since the second set of composites is based on a unidimensional variation of zonally averaged SIF over the GrSea, all grid cells of composited variable essentially contain the average over the same subset of days (i.e., d_+ and d_- are the same for all grid cells).

335   We applied the nonparametric Wilcoxon rank-sum test to detect statistically significant differences between high and low composites of STG and SIF. This method tests at each grid point the local null hypothesis $H_o: V_+(lon, lat) = V_-(lon, lat)$ at a 95 % confidence level.

3 Results

The changes in T_{2m} and the resulting STG can be attributed to a large number of different drivers. Here, we explored the seasonality of the STG in the ZR and the variables influencing the STG. Along with the local factors like surface type and fjord-ice condition, STG anomaly is triggered by various large-scale factors.

3.1 Slope temperature gradient

The near-surface climate is influenced by its surface characteristics (e.g., the occurrence of snow, bare soil, vegetation, etc). The inclusion of the UAV-based air temperature profiles, which represent the vertical temperature gradient, helps to discern a comprehensive perspective of temperature variability in the ZR and complements the results. Figure 3 gives a general overview of seasonal mean temperature profiles from AWSs and UAV for temporally overlapping periods between the stations. Note, that all UAV-based measurements are made during the summer months. During the UAV measurement in the summer of 2017, the valley was covered by snow, and foggy conditions prevailed, whereas, during the measurement in the summer of 2018, there was scattered snow cover. The average temperature profile from the UAV measurements in the summer of 2017 is marked by the presence of strong inversions, and it is distinct from the rest of the average summer temperature profiles from the AWSs (Figs. 3 and S1).

The ZAC and M3 stations were used for comparison of the sub-daily vertical temperature gradient from the UAV and STG (Fig. S1). There is a close correspondence between the UAV and the AWS temperature measurements at the same elevation (R^2 = 0.8–0.9, $p < 0.05$; Fig. S1). Notably, the temperature difference (M3 minus ZAC) calculated from AWSs and the corresponding UAV-based measurements show a significant correlation (R^2 = 0.7–0.9, $p < 0.05$) with the mean absolute error (MAE) of 0.6–1.0 °C. This highlights the potential of AWSs to capture the inversions in the ZR, despite the surface characteristics influencing screen-level temperature.

Nonlinear temperature profiles are evident during the winter season, in which temperature increases vertically at lower elevations (i.e., ~43–420 m a.s.l., ZAC–M3) indicating the presence of inversions and then gradually decreases further up (Fig. 3). During winter, at the APO (where AP1, AP2, and AP3 are located), the temperature decreases with elevation and the STGs are consistently shallower than the vertical ELR ($STG_{AP2-AP1}$ = -2 ºC km^{-1} and $STG_{AP3-AP2}$ = -5 ºC km^{-1} versus -6.5 ºC km^{-1}).
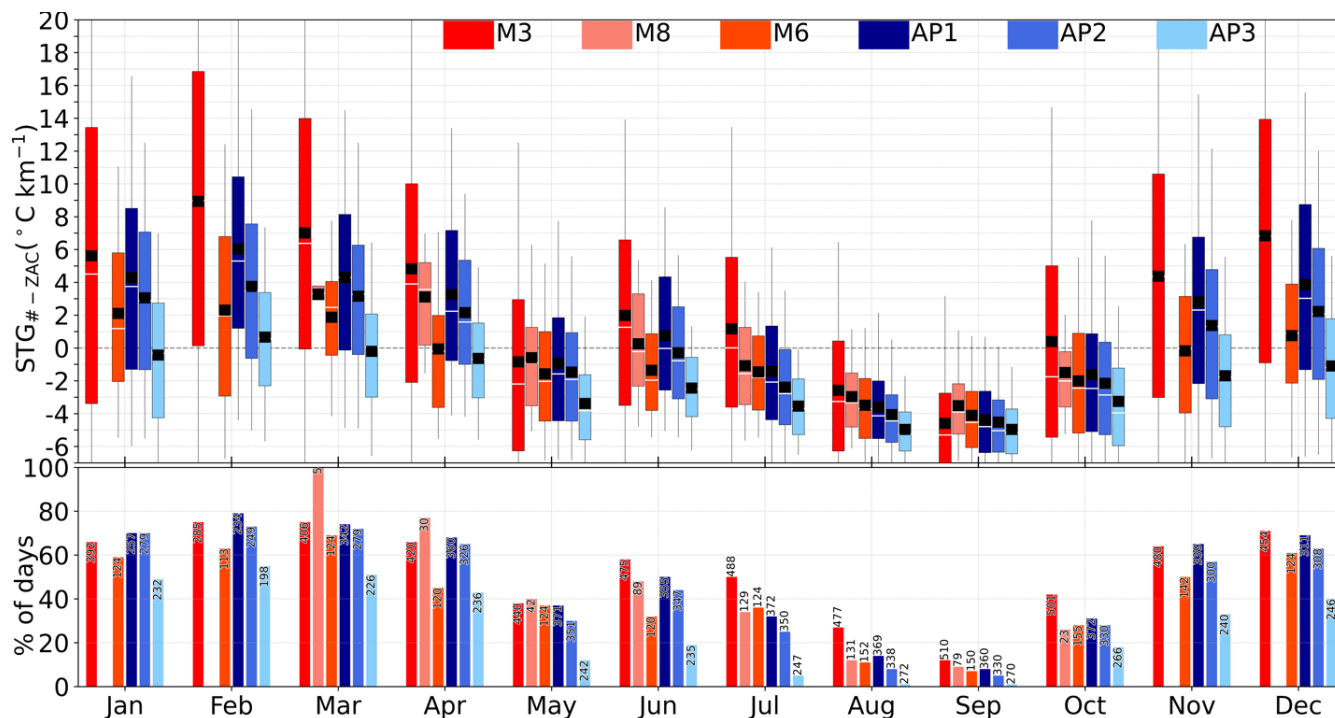
Figure 4. Annual cycle of monthly STG (°C km^{-1}) between ZAC and other higher AWSs (# indicates stations listed in the legend). The upper panel shows the boxplot of daily mean STG for each month, and the lower panel shows the frequency (% of days) of positive STG (i.e., inversion days) in total measurement days (number inscribed on or at the top of the bar plot)

Figure 4 shows the annual cycle of the daily average STGs between ZAC and other AWSs for each month for different temporal resolutions (sample size inscribed in the bar plot). As expected, winter (DJF) is dominated by the strongest inversions (more positive STG), whereas inversions become weaker (less positive STG), and less frequent as the summer (JJA) approaches. The strongest (mean = ~14 °C km^{-1}; 25th–75th percentiles = 7–20 °C km^{-1}) and most frequent (~75 % of 285 days) inversions are present within the ZR in February, especially between ZAC and M3, which have an elevation difference of 377 m (Figs. 3 and 4). Above M3 elevation (e.g., M6), inversions (positive STG$_{M6-ZAC}$) become weaker (6 °C km^{-1}) and less frequent (63 % of 113 days), however, the period used to calculate STG$_{M6-ZAC}$ does not necessarily overlap with the STG$_{M3-ZAC}$ period. Nevertheless, a similar pattern was observed when overlapping days for ZAC, M3, and M6 stations were considered to calculate STGs (for winter 356 overlapping days: STG$_{M3-ZAC}$ = 12 °C km^{-1}, 70 %, and STG$_{M6-ZAC}$ = 5 °C km^{-1}, 61 %). Also, during winter, strong and frequent positive STG exists between ZAC and stations on APO (especially AP1; mean positive STG$_{AP1-ZAC}$ = 8 °C km^{-1}, ~72 % of 802 days), (Figs. 3 and 4).

As spring (MAM) and (early) summer approach, inversions within the valley gradually become weaker and less frequent (Figs. 3 and 4). During spring, the mean positive STG$_{M3-ZAC}$ is ~9 °C km^{-1} (4–14 °C km^{-1}), and the frequency of inversions is 59 % of 1131 days. In summer, particularly during the snow-free period, STG becomes steeper, however, mean STG$_{M3-ZAC}$ still shows a positive gradient (1–2 °C km^{-1}) for 45 % of 1440 days. In September, STGs are steepest (most negative, -5.0–-3.5 °C km^{-1}), and inversions are rare (1–12 % of days); when the valley is completely snow-free and

prevailing positive net radiative balance promotes mixing (Figs. 3 and 4). Hence, the temperature decreases with elevation in the entire valley system.

385   One of the main factors influencing the T_{2m} via the energy balance is the surface type. The spatial distribution of snow on the ground can impact the vertical temperature gradient (Kirchner et al., 2013) as well as STG. The daily mean STG_{M3-ZAC} when snow is present (mean = 4 °C km^{-1}; 25th–75th percentiles = -4–10 °C km^{-1}) and absent (-0.3 °C km^{-1}; -5–3 °C km^{-1}) at both stations is significantly different (p < 0.01), (Fig. S5). When snow is present at both stations, the daily mean STG_{M3-ZAC} is shallowest and most positive (4 °C km^{-1}) compared to STG_{M3-ZAC} when snow is absent either at ZAC (-4 °C km^{-1}) or at

390   both stations (-0.3 °C km^{-1}). However, the difference was not statistically significant (p = 0.5 at the 0.05 significance level) between STG_{M3-ZAC} when snow is present at both stations and only at ZAC (2 °C km^{-1}), which keeps the valley bottom (surface) cold, favoring inversions. In contrast, STG_{M3-ZAC} is steepest (-4 °C km^{-1}) when snow is present only at M3, which causes the temperature to decrease with elevation. This highlights the importance of snow, which governs the evolution of STG in the ZR.
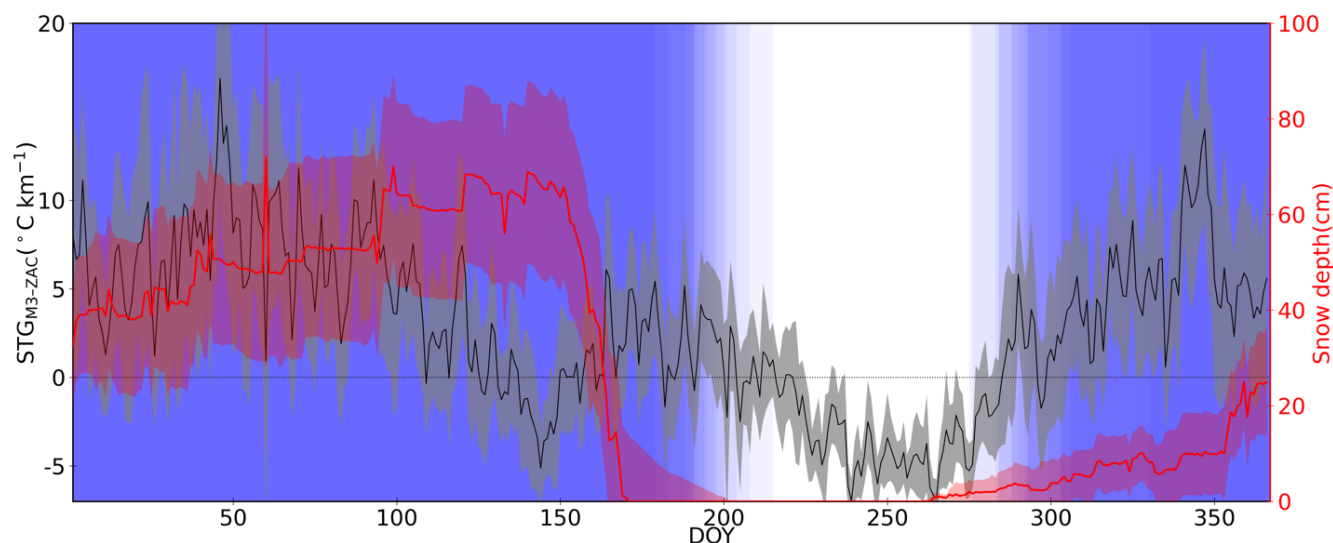
395

Figure 5. Annual cycle of STG between ZAC and M3 (STG_{M3-ZAC} in °C km^{-1}) and snow depth (in cm) measured at ZAC for 2004–2019. The black and red lines denote the daily mean STG_{M3-ZAC} and snow depth, and the grey and red shaded area denote a 95 % confidence interval around the given mean, respectively. The blue shades in the background mark day of the year (DOY) when ice was present in Young Sound for the period 2004–2019. Fainter blue shade indicates the transitional period (ice break-up–open

400   **water or open water–ice formation) of fjord-ice**

        Another local factor that can influence the temperature anomaly in the ZR is the fjord-ice break-up and formation period in Young Sound (Figs. 1 and 5). Figure 5 depicts the annual cycle of daily mean STG_{M3-ZAC} and snow depth, and the condition of fjord-ice. Even though the STG is strongly controlled by the surface type (presence and absence of snow), the temporal evolution of fjord-ice can amplify or reduce the prevailing climate anomaly. The shallowest STG_{M3-ZAC} is observed

405   when Young Sound is completely covered by ice whereas the steepest STG_{M3-ZAC} when the fjord was ice-free. A similar

annual relationship was observed between $STG_{AP1-ZAC}$ and the condition of fjord-ice (not shown) implying that the fjord-ice-related anomaly is largely dominated within the surface layer close to ZAC.

3.2   Physical controls of STG

To test the hypothesized potential relationship between the STG in the ZR and large-scale drivers, we utilized synthesis of
410   observations (AWSs), reanalysis (ERA5), and RACMO. In particular, the potential relationships between the STG, Z500, U_{10m}, surface and atmospheric moistures, SIF, and surface mass balance (SMB) of the APO were explored.

3.2.1   Large-scale atmospheric circulation
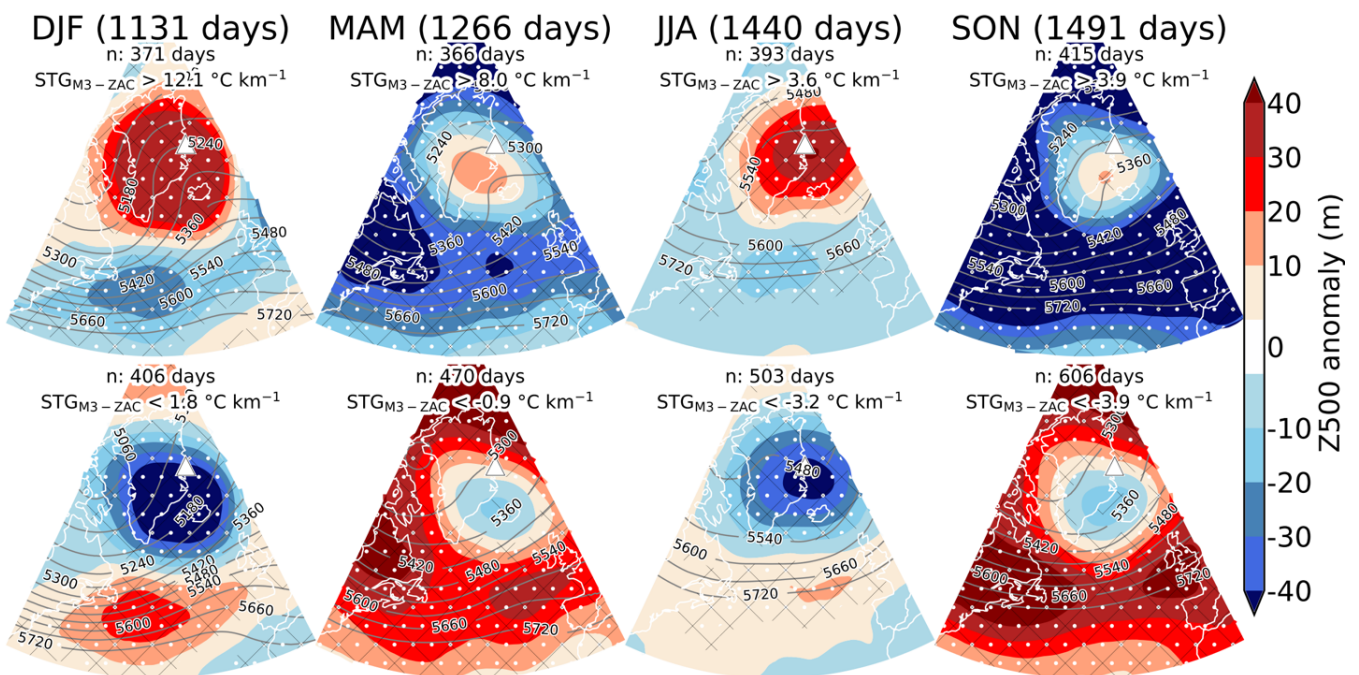
Figure 6. Composite of geopotential height at 500 hPa (Z500 in m) anomalies (shading) and means (grey contours; 60 m interval)
415   **from ERA5 corresponding to the STG between M3 and ZAC (STG_{M3-ZAC}) for entire daily measurements (number of days indicated at the top of each seasonal column) for a given season (2004–2019). The upper and lower panels represent Z500 anomaly and mean corresponding to high and low STG days i.e., n number of days when STG_{M3-ZAC} exceed and is less than the indicated STG values in °C km⁻¹, respectively, for the given season. The triangle represents the location of the Zackenberg region. The white dots and areas within the black mesh indicate statistically significant differences between high and low composite anomalies at the**
420   **0.05 and 0.1 significance levels, respectively**

The role of the large-scale atmospheric circulation in the variation of STG are investigated by a composite analysis. Figure 6 represents composite anomalies of Z500 corresponding to high ($STG_{M3-ZAC} > STG_\mu + 0.5\,STG_\sigma$) and low ($STG_{M3-ZAC} < STG_\mu - 0.5\,STG_\sigma$) STG days between M3 and ZAC (STG_{M3-ZAC}) for a given season (2004–2019). Note the similarities between the seasonal anomaly patterns for both the high and low STG days, and the contrast between high and
425   low STG days for a given season. Shallower (steeper) STGs are associated with a positive (negative) anomaly in Z500

relative to the seasonal mean (2004–2019) over eastern Greenland. A similar pattern is observed over the GrSea, but only during winter and summer. An opposite anomaly pattern of Z500 is observed over the southern (equatorward) node of the NAO (where the Azores High resides). Furthermore, the southerly wind pathway is shifted to the northwest (upper-air ridging) and southeast direction during high and low STG$_{M3-ZAC}$ days, respectively (Fig. 6). The positive (negative) anomaly

430 of Z500 over the ZR indicates that the upper air (~5500 m) is warmer (colder) than the mean atmospheric state, which leads to shallower (steeper) STG$_{M3-ZAC}$ than the mean STG$_{M3-ZAC}$ (Fig. 6). Hence, along with the surface-bound factors such as snow, and topographic shading, and as excepted, the temperature gradient within the ZR is dependent on synoptic conditions.

When replacing STG$_{M3-ZAC}$ with data from other stations, e.g., STG between M6 and ZAC, and AP1 and ZAC (not

435 shown), etc., the relationship to Z500 anomalies remains unchanged. Also, using all the aforementioned criteria to isolate the composites result in a similar anomalies pattern (not shown). This implies that the method used in this study can detect a robust statistical linkage between STG and atmospheric circulation patterns.

The anomaly composites of P$_{surf}$ corresponding to high and low STG$_{M3-ZAC}$ days show a similar pattern as Z500, while the centers of both anomalies are shifted eastward (Fig. S6). The shallower (steeper) STG$_{M3-ZAC}$ is associated with higher

440 (lower) P$_{surf}$ compared to the seasonal mean (2004–2019) over the ZR. This implies that STGs are steeper (shallower) in the case of cyclonic (anticyclonic) circulation patterns. The negative anomaly of P$_{surf}$ does not necessarily imply the cyclonic condition over the ZR (Fig. S6). However, it indicates below average P$_{surf}$, which is also in line with P$_{surf}$ anomaly measured at ZAC for high (0.2–4.1 hPa) and low (-4.5–-0.5 hPa) STG$_{M3-ZAC}$ days. This means that large-scale synoptic patterns are in line with local measurements.

445
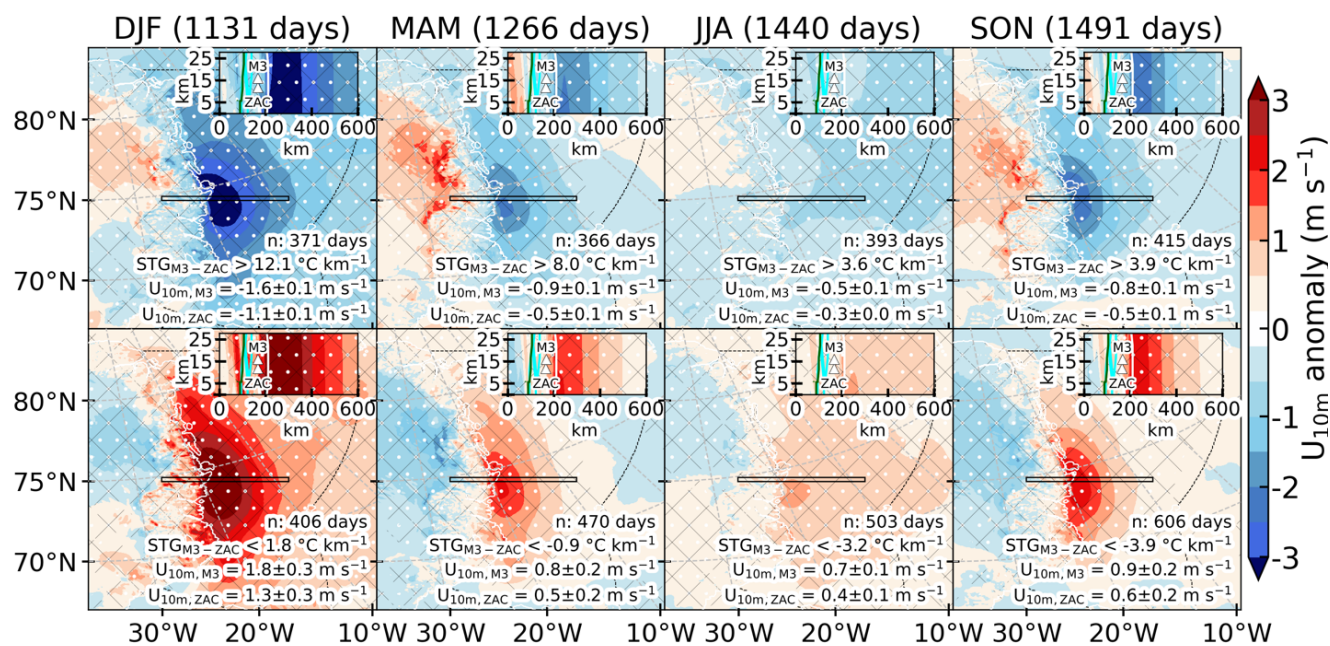
Figure 7. Idem as Fig. 6, but for the composite of wind speed at 10 m (U_{10m} in m s^{-1}) anomalies from RACMO. The inset figure shows the zoomed-in version of the black rectangle in the main figure and Fig. 1 encompassing the ZR; the location of the stations (triangle), the land-sea border (white contour), peripheral glacier (cyan contour), and the GrIS (green contour) are indicated in the inset figure. The dashed black line represents the GrSea coverage. The mean U_{10m} anomaly values (in m s^{-1}) interpolated to the station location are also shown in the lower right corner indicating a 95 % confidence interval (calculated using bootstrapping methods). The white dots and areas within the black mesh indicate statistically significant differences between high and low composite anomalies at the 0.05 and 0.1 significance levels, respectively

As another source of impact, the vertical temperature gradients are controlled by the vertical atmospheric mixing strength and thus a strong relationship between STG and U can be expected (Pepin, 2001). Steeper (shallower) STG_{M3-ZAC} are associated with higher (lower) U_{10m} at both stations (Fig. 7). At both stations (M3 and ZAC), the observed U_{2m} anomaly is similar to the anomaly pattern shown by RACMO using the same reference period (Table S4). Note that the U_{10m} over the GrSea (closest to the study area) consistently shows a similar anomaly pattern as in the ZR (Fig. 7) indicating a similar effect of the U on the STG both over water and coastal region. Findings are independent of station pairs used for characterizing STG (not shown). The strongest inversions (positive STG_{M3-ZAC}) are observed for an average U_{2m} of 2–4 m s^{-1} (Fig. S7). However, as the U_{2m} increases above 4 m s^{-1}, the STG_{M3-ZAC} becomes steeper (and inversions are weakened).

3.2.2   Near-surface and atmospheric moistures

The shallower STG_{M3-ZAC} is associated with lower q_{2m} over the GrSea compared to the reference seasonal mean over water except for summer (not shown). The computed (from station) and interpolated (from RACMO) q_{2m} anomalies depict a similar pattern with respect to the same baseline period (Table S4).

On average, the inversion strength (positive STG) decreases (less positive or negative) with increasing CCF by enhancing the emission of the LWR_{in} (Nielsen-Englyst et al., 2019). During the high (low) STG_{M3-ZAC} days, the CCF is less (more) in the ZR (Table S4). The computed CCF anomaly is in line with the result from RACMO.

Cloud microphysical composition (such as ice and liquid water cloud content) is radiatively more important than CCF
470 to the near-surface climate. The change in cloud content affects the cloud optical thickness and the integrated precipitation over Greenland (Noël et al., 2018), and hence, can potentially affect the STG over the ZR. Therefore, we explore the association between the daily IWP and LWP, and STG. We find that during high (low) STG_{M3-ZAC} days both IWP and LWP is smaller (larger) than the baseline average (not shown).

Weather conditions such as precipitation events dampen the inversion strength i.e., steepens the STG, by favoring
475 turbulent mixing through atmospheric convection or orographic lifting. We find that both solid (snow) and liquid (rain) precipitation from RACMO is higher (lower) during low (high) STG_{M3-ZAC} days (Fig. S8).

3.2.3 Fractional sea-ice cover
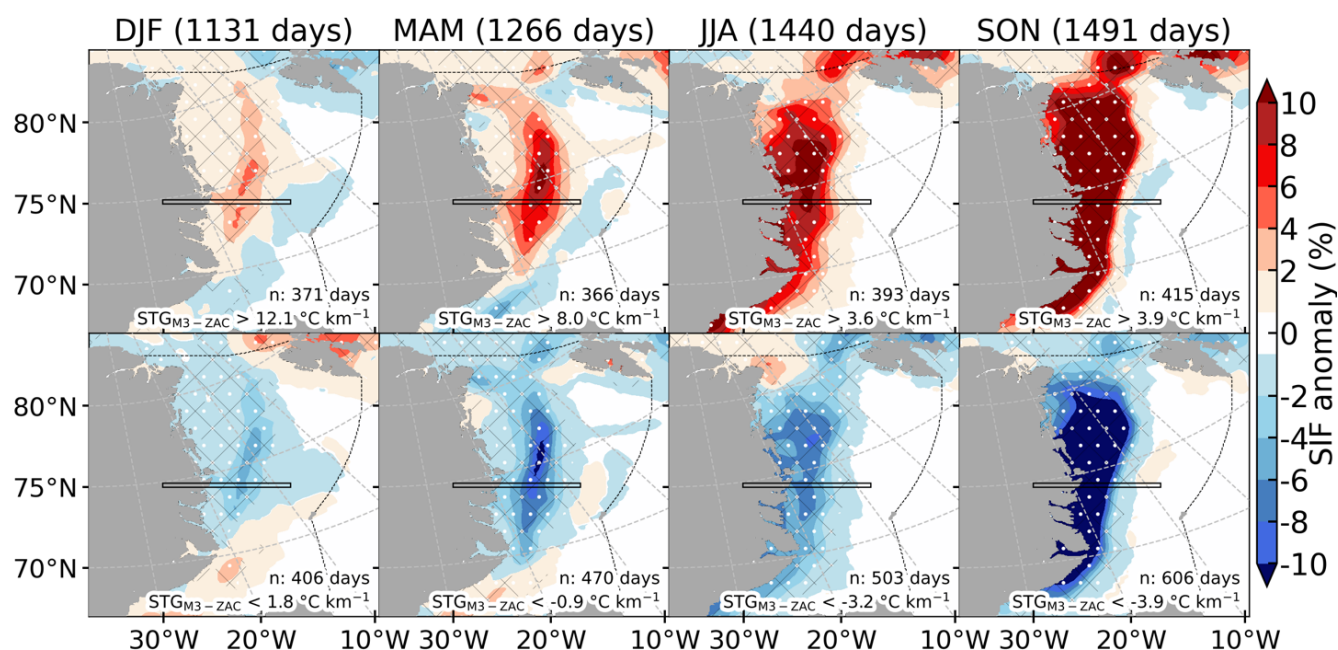
Figure 8. Idem as Fig. 7, but for the composite of fractional sea-ice cover (SIF in %) anomalies from ERA5 interpolated to the
480 **RACMO grid**

Above we show that large-scale patterns relate consistently to local atmospheric stability conditions in the ZR. As a next driver, we assess the variability of SIF, its export through the GrSea, and its role for local weather conditions in the ZR (Hansen et al., 2008). Figure 8 presents the composites of SIF corresponding to the STG in the ZR. This result implies a link between STG and variability in SIF, suggesting that the shallower (steeper) STG_{M3-ZAC} is associated with higher (lower) SIF

485   in the GrSea (2004–2019). Also, the steepest STG is recorded in September (Fig. 4) which is also the month of the lowest
sea-ice extent (Fig. S4). A similar pattern of SIF composite was observed while using other station pairs (not shown).

3.3   Impact of sea-ice variability

To assess the impact of SIF on atmospheric conditions, and hence the STG in the ZR, high spatiotemporal resolution datasets
are needed. We separated the atmospheric variables corresponding to high and low SIF days in the GrSea (Fig. S9). The
490   result shows that the greatest variability in the atmospheric variable is close to the area of marginal sea ice in the GrSea (Fig.
S9). Composites of atmospheric variables at each grid point of RACMO based on high and low SIF were created. As a
result, the first part of the analysis is limited to the regions covered by sea ice to identify signals in atmospheric phenomena
due to local changes in SIF.

Over the GrSea, high (low) SIF is associated with higher (lower) than normal P_{surf} (Fig. S10). The open water surface
495   favors more evaporation, decreasing the P_{surf} over the sea. The reduction in the P_{surf} associated with low SIF can enhance the
convection over the open water surface and associated moisture flux for precipitation. As a result, low SIF corresponds to
increased q_{2m} and precipitation amounts over the sea (Figs. S11 and S12). Furthermore, the low U_{10m} coincides with the high
SIF over the GrSea (Fig. S13). This result is in line with Jakobson et al. (2019) who found a negative correlation between
SIF and U over the Arctic Ocean (particularly in autumn, winter, and spring) which reflects the reduction in atmospheric
500   stratification and aerodynamic surface roughness associated with a decrease in SIF. Note that similar patterns for P_{surf},
precipitation, and U_{10m} were observed over the GrSea for the high and low STG days in the ZR (Figs. S6, S8, and 7 versus
Figs. S10, S12, and S13), which supports the fact that sea ice plays a strong role in influencing lapse rates by controlling the
atmospheric conditions in the valley.

Table 2. Mean anomalies of 2 m air temperature (T_{2m} in ºC) and the slope temperature gradient (STG_{M3-ZAC} in ºC km⁻¹) between
505   **M3 ($T_{2m, M3}$) and ZAC ($T_{2m, ZAC}$) pair corresponding to high and low fractional sea-ice cover (SIF in %) from ERA5 averaged over**
the Greenland Sea for the given season (2004–2019). $T_{2m, M3}$, $T_{2m, ZAC}$, STG_{M3-ZAC}, and SIF anomalies are calculated using the same
period i.e., when the variable is recorded by both AWSs

Seasons	DJF		MAM		JJA		SON	
Composites	High	Low	High	Low	High	Low	High	Low
Total days	1131		1266		1440		1491	
SIF (days)	41 (57)	-26 (76)	35 (64)	-36 (64)	33 (72)	-6 (908)	33 (75)	-5 (1043)
$T_{2m, M3}$	-2.2	2.9	-3.9	5.6	-1.1	0.4	-5.8	2.3
$T_{2m, ZAC}$	-3.5	4.3	-6.1	7.3	-2.9	0.9	-7.4	3.2
STG_{M3-ZAC}	3.6	-3.6	5.8	-4.4	4.7	-1.2	4.3	-2.2

In the second part of the analysis, we again divided STG and atmospheric variables according to high and low SIF
zonally averaged over the GrSea (blue shaded area in Fig. 1), (Fig. S4). This was done to understand how the change in SIF

510 over the GrSea on average affects the atmospheric conditions in the near-coastal (terrestrial) area, in particular the ZR. The results show that during high (low) SIF days over the GrSea, the STG in the ZR is shallower (steeper) than the mean values (Table 2); the mean STG_{M3-ZAC} varies by $\sim$4 ºC km^{-1} for a corresponding $\sim$27 change in SIF over the GrSea. Both stations show a negative (positive) anomaly of T_{2m} corresponding to the high (low) SIF days (Table 2). However, on high SIF days, the lower (e.g., ZAC) station shows more negative anomaly ($\sim$-5 ºC) compared to the higher station (e.g., M3; $\sim$-3 ºC),

515 shallowing the STG; the opposite is true for the low SIF days, thus, steepening the STG. Other station pairs also showed similar results, e.g., during high SIF days (24–34 SIF anomaly) the STG_{M6-ZAC} is more than the mean value (1.5–2.7 ºC km^{-1}), while during low SIF days (-33--6 SIF anomaly) the STG_{M6-ZAC} is relatively less (-1.7--0.6 ºC km^{-1}) than the mean (Table S5).

The temperature difference (ΔT) between the outer (DAN's location) and inner coast (ZAC's location) is also impacted

520 by the change in sea ice. The aerial distance between the outer coast and stations increases in the following order: DAN (2 km) < ZAC (27 km) < M7 (32 km), (Fig. 1). Generally, along the Young Sound (fjord), a strong temperature (and pressure) gradient develops which generates onshore winds (especially in summer, Fig. S3); in winter the mesoscale wind field (northerly wind) dominates. In winter, the outer part of the fjord is warmer than the inner coast ($\Delta T_{DAN-ZAC}$, $\sim$1 ºC for 1996–2015), which indicates the maritime influence due to the existence of partially open water at the opening of Young Sound (Hansen et al., 2008). Summertime, however, is characterized by an opposite temperature gradient ($\Delta T_{DAN-ZAC}$ $\sim$-0.7 ºC for

525 1996–2015); the cold GrSea and drifting sea ice make areas near the ocean colder than snow-free inland areas. The continentality increases rapidly towards inland (ΔT_{DAN-M7} $\sim$-3--1 ºC for 2009–2015). Interestingly, $\Delta T_{DAN-ZAC}$ shows a consistent anomaly during the high and low SIF days for all seasons; the $\Delta T_{DAN-ZAC}$ is higher (lower) than the mean for high (low) SIF days (Table S5). This implies that areas near the coast (DAN) are warmer (colder) than inland (ZAC) during high

530 (low) SIF days. The reason for the observed anomalous pattern in continentality might be due to warmer and fresher surface water being trapped in the inner part of the fjord due to a high SIF (or multi-year sea ice), as reported by Stranne et al. (2021) in a fjord in North Greenland and possibly increasing the local temperature. Moreover, the sea-ice damming effect might influence the outer part of the fjord more than the inner part, causing a positive (negative) coast-inland temperature gradient anomaly during high (low) SIF days.

535
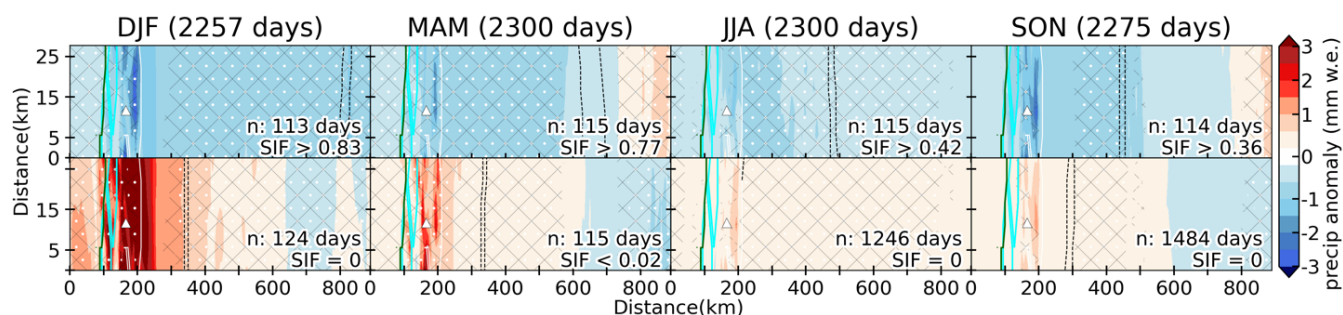
Figure 9. Composite of precipitation (precip in mm w.e.) anomalies from RACMO corresponding to zonally (overall grid cells) averaged (median) SIF over the Greenland Sea for entire daily measurements for the given season (1996–2020). The upper and lower panels represent precipitation anomaly corresponding to high and low SIF days i.e., n number of days when SIF exceed and is less than or equal to the indicated SIF values, respectively, for each season. The figure is the zoomed-in version of the black rectangle in Fig. 1 encompassing the ZR; the location of the stations (triangle), the land-sea border (white contour), peripheral glacier (cyan contour), and the GrIS (green contour) are indicated. The average sea-ice extent (dashed black line) for the given condition is also shown; the outer line represents 0.25 SIF and the inner line 0.3. The white dots and areas within the black mesh indicate statistically significant differences between high and low composite anomalies at the 0.05 and 0.1 significance levels, respectively

The change in the SIF has a similar impact on the terrestrial climate of the ZR as it has over the GrSea. On high SIF days, the sea-ice extends ~600 km east of Zackenberg while on low SIF days, it extends ~100 km east (Fig. 9) on average. This can have several implications on Zackenberg's climate. Over the ZR, the T_{2m} anomaly composite from RACMO (Fig. S14) shows a similar pattern as observed by the climate station (Table 2) for days with a high and low SIF. Also, both calculated and interpolated q_{2m} anomaly composites show a consistent pattern for high and low SIF days (Table S6). The enhanced atmospheric instability (convection), availability of moisture, and increase in U_{10m} associated with reduced SIF and its extent bring more precipitation to the ZR (Fig. 9), and consequently, the STG becomes steeper.
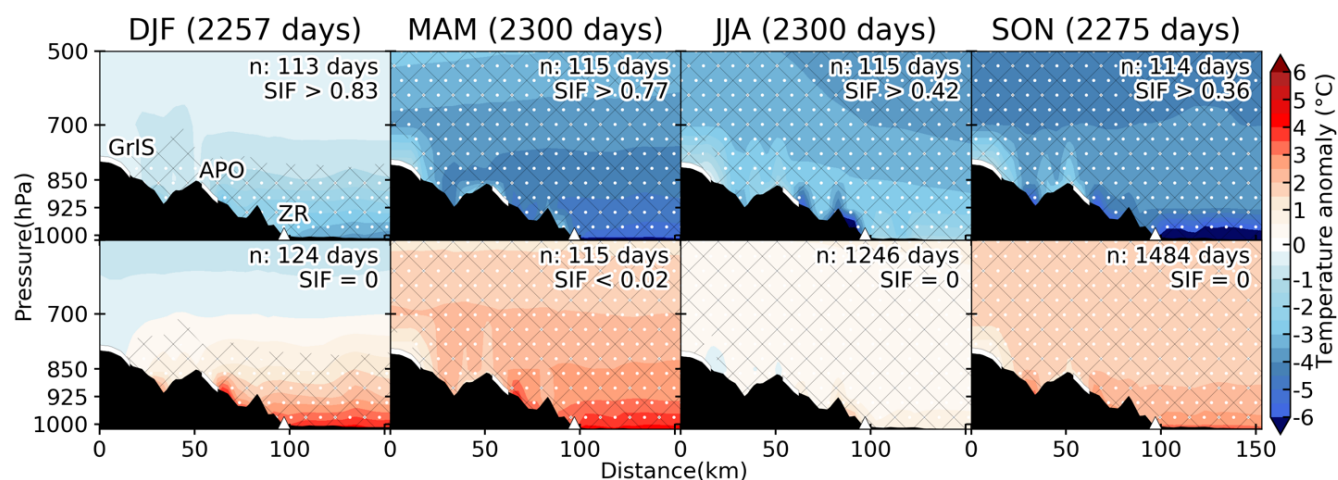
Figure 10. Idem as Fig. 9, but for the composite of the cross-sectional transect (XY as shown in Fig. 1) of vertical air temperature (T in °C) anomalies profile. The portions of the Greenland Ice Sheet (GrIS), A. P. Olsen Ice Cap (APO), and the Zackenberg region (ZR) passing through the transect are labelled in the upper panel of DJF season.

To understand how the SIF variability affects the vertical temperature gradient, we further divided the vertical atmospheric variable along the XY transect shown in Fig. 1 (Fig. 10). Evidently, the SIF variability causes a nonlinear vertical response; it has a stronger influence in the low-level atmosphere compared to the upper level. Mostly, the negative

560 (positive) anomaly of temperature is associated with high (low) SIF days. However, the temperature anomaly is more negative (positive) in the low-level atmosphere close to sea ice compared to the upper-level for high (low) SIF days. On average, when SIF increases by 48, the temperature decreases by -7 ºC at 1000 hPa and -3 ºC at 500 hPa along the transect, and when SIF decreases by 37, the temperature increases by 4 ºC at 1000 hPa and 0.7 ºC at 500 hPa along the transect (Fig. 10). This result suggests that the variability of SIF has a greater impact on the air close to the surface than higher above.
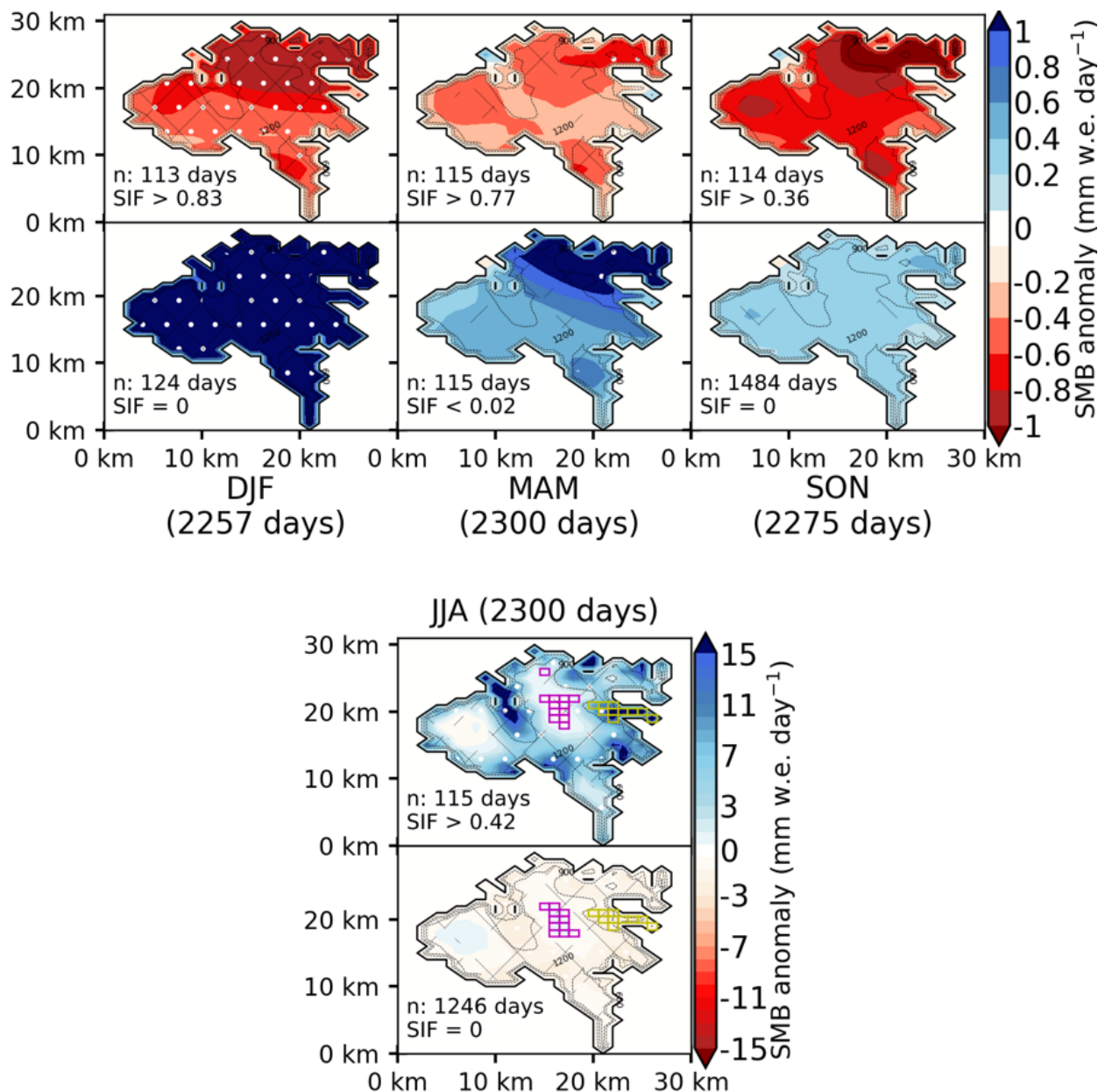
Figure 11. Idem as Fig. 9, but for the composite of daily surface mass balance (SMB in mm w.e. day⁻¹) anomalies of A.P. Olsen Ice Cap (APO), (location in Fig. 1) from RACMO. In JJA panel, the magenta and yellow rectangles indicate the grid cells whose values are used for the calculation of the average SMB anomaly on accumulation (>1100 m a.s.l.) and ablation (<1100m a.s.l.; only the southeastward flowing outlet glacier) area, respectively, of the APO. Note the use of a separate color bar for summer composite due to large mass overturn

An interesting question related to the STGs and their connection to the SIF, is the effect on the energy or mass balance of the local glaciers and ice caps. We examined the SMB of the APO from RACMO to assess the relevance of the STG and SIF variability for estimating the SMB of the glacier. Our main focus is the southeastward flowing outlet glacier as long-

term atmospheric and glaciological measurements exist there (Citterio et al., 2017). We used an equilibrium line altitude
(ELA) of 1100 m a.s.l. following Noël et al. (2019) to estimate a typical separation between accumulation and ablation areas
of the APO. For all seasons except summer, the daily mean SMB is less (more) than the reference SMB (1996–2020), (Fig.
S15) during high (low) SIF days (Fig. 11). This is true for both the accumulation and ablation area of the APO. For high SIF
days, the reduction of daily SMB (-0.8–-0.5 mm w.e. day^{-1}) can be attributed to the reduction in precipitation and q_{2m},
leading to less accumulation of snow (Fig. S16); conversely, the increase in precipitation (in the form of snow) and q_{2m}
associated with low SIF could increase SMB (0.3–2.2 mm w.e. day^{-1}). Furthermore, despite T_{2m} being higher than the
reference during days with low SIF, T_{2m} remains largely negative (Fig. S17) and does not lead to increased melt, but
increased snowfall rates (Schweiger et al., 2008).

The summer SMB anomaly pattern is different from the rest of the season in that anomalies show a different signal in
the accumulation and ablation areas (Fig. 11). Overall, the SMB anomaly becomes more negative (positive) with elevation
on high (low) SIF days. In the ablation area of the APO, the positive anomaly of SMB (~16 mm w.e. day^{-1}) is related to high
SIF days, indicating less melt than on average. In contrast, for low SIF days, the SMB over the ablation area shows a
negative anomaly (~-3 mm w.e. day^{-1}), indicating more melting. The decrease (increase) in T_{2m} associated with high (low)
SIF days, which reduces (enhances) the melt rates, can possibly explain the resultant positive (negative) SMB anomaly in the
ablation area; for high (low) SIF days T_{2m} anomaly is -2 (~0.01) ºC. Also, the positive anomaly of the LWR_{in} (related to an
increase in atmospheric moisture and liquid bearing cloud) (not shown) associated with low SIF days can further explain the
negative SMB anomaly.

In the accumulation area of the APO, the summer SMB anomaly pattern shows a vertical gradient; in high (low) SIF
days, the SMB anomaly changes from positive (negative) to negative (positive) value with elevation. On average, the SMB
anomaly is positive (negative) for high (low) SIF days in the accumulation area. However, the anomaly sign changes with
elevation. In higher reaches of the accumulation area (above ~1317 m a.s.l.), for high SIF days the daily mean SMB is less
than the reference SMB (~-0.3 mm w.e. day^{-1}); for low SIF days, the SMB anomaly is ~0.06 w.e. day^{-1} (above ~1157 m
a.s.l), (Fig. 11). The decrease (increase) in precipitation associated with high (low) SIF days leads to less (more)
accumulation of snow, and hence less (more) SMB with respect to the baseline mean.

4   Discussion

The STG in the ZR shows a pronounced seasonal cycle, with the strongest inversions (positive STG) occurring mostly in
winter (Fig. 4). The formation of temperature inversions in the ZR is mainly due to radiative cooling of the snow surface,
particularly during polar night (Hansen et al., 2008; Shahi et al., 2020). Moreover, ZAC shows the lowest mean winter T_{2m}
(~-19 ºC) compared to stations higher up for all overlapping periods (Fig. 3). Thus, the ZAC location (valley bottom) might
represent the approximate elevation of the inversion base (lowest elevation of the inversion layer), especially during winter.

605 The occurrence of sporadic rain and breeze, which cause mixing of the lower atmosphere can dissolve the inversions (Fig. S1b).

During winter, strong and frequent positive STG between ZAC and stations on APO can be attributed to cold air pooling in the valley, resulting in temperature inversions within the valley, whereas the APO remains above the inversion layer. Clearly, this information is imperative in the glacier mass balance modeling perspective for simulating temperature on
610 the glacier back in time using the longest recorded information from ZAC.

Spring and (early) summertime inversions in low-lying coastal regions like the ZR can be attributed to the cooling of the atmospheric layers above the surface due to the consumption of energy for snowmelt (Serreze and Barry, 2014). During summer, STG on the valley floor might be influenced by low-level marine stratus clouds brought by the prevailing sea breeze from the outer coast (Hansen et al., 2008), (Fig. S3). Furthermore, the base of low clouds (fog) on the mountain
615 slopes can also increase due to the mixing within the lower atmosphere, which can lift the inversion base from 300 to 600 m by advection and create elevated inversions (inversions whose base is above the surface), (Hansen et al., 2008).
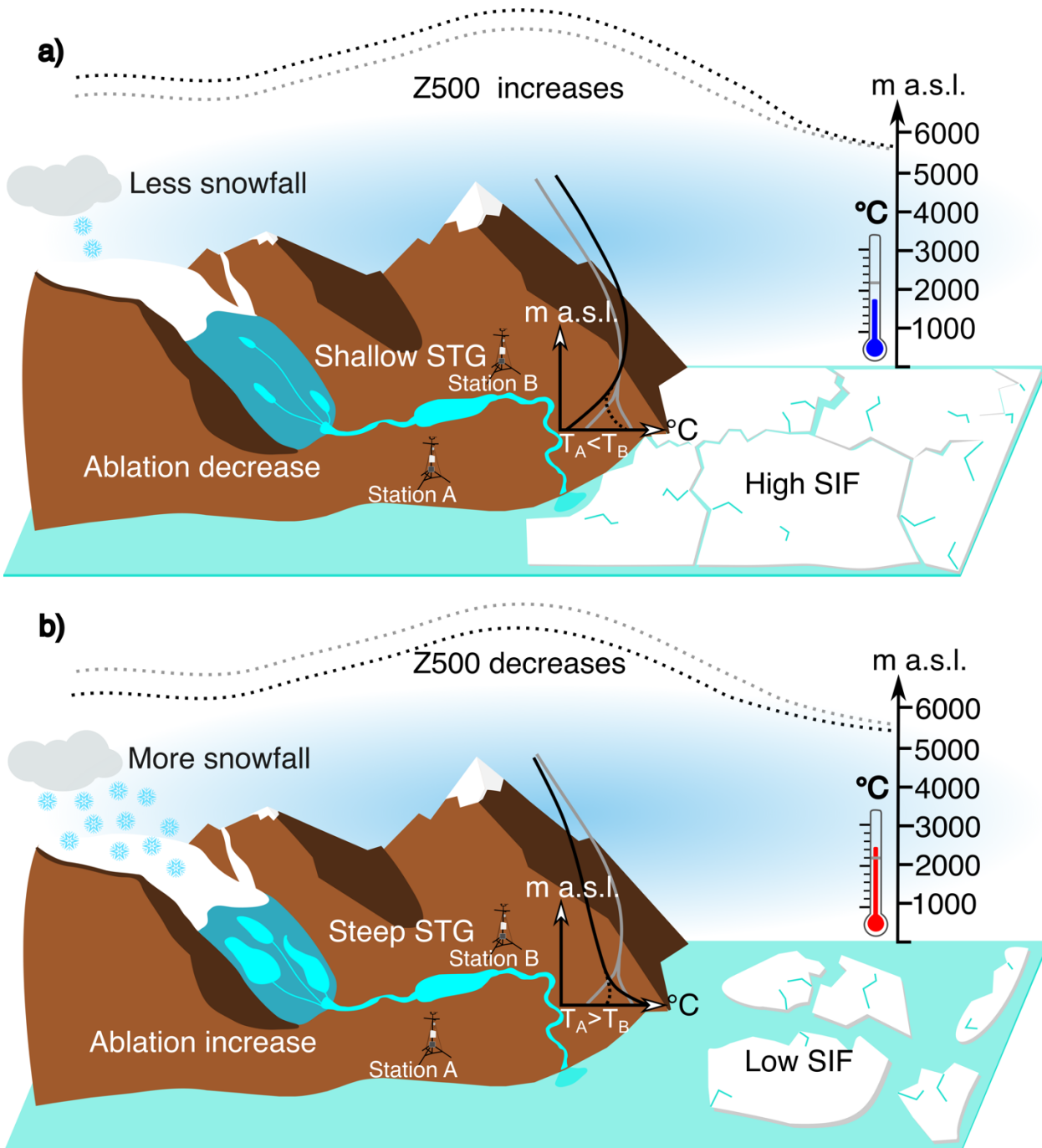
Figure 12. A schematic diagram of some important linkage between slope temperature gradient (STG) in the Zackenberg region (ZR), fractional sea-ice cover (SIF) in the Greenland Sea, surface condition of A. P. Olsen Ice Cap (APO), and geopotential height at 500 hPa (Z500). Station A is situated at lower elevation than station B; temperature at station A (T_A) can be higher or lower than temperature at station B (T_B). (a) The upper panel shows the condition when STG_{B-A} is shallow (T_A is less than T_B; less negative or positive (inversion) STG_{B-A}), SIF is high, Z500 increases, less snowfall, and less snow/ice ablation in APO. (b) The lower panel shows the opposite condition when STG_{B-A} is steep (T_A is more than T_B; more negative or less positive STG_{B-A}), SIF is

low, Z500 decreases, more snowfall, and more snow/ice ablation in APO. The grey lines represent a climatological mean of Z500
(dotted line at the top) and temperature profile (solid line in the middle) in the ZR. The corresponding black lines represent the
mean Z500 (dotted line at the top) and temperature profile in each condition. The dotted line of the temperature profile
corresponds to the least favorable temperature profile in the given condition. The blue and red color thermometers indicate that
the average temperature is less and more than the climatological mean, respectively, for each condition

Figure 12 shows the comprehensive picture of the potential relationship between the STG, Z500, SIF, and SMB of the APO analyzed in this study. The Z500 composites we use to attribute days with high and low STG do not necessarily correspond to GBI anomalies since a large area is averaged (60–80° N, 20–80° W region) to derive the latter. We elaborate on the variations of STG at the local scale in response to the spatial variability of composites anomaly of Z500. The positive (negative) anomaly of Z500 strengthens (weakens) the Greenland anticyclone, which increases (decreases) the downward vertical motion of air, consequently leading to positive (negative) air temperature anomalies (Fig. 12). Locally, we find that this effect is stronger in higher elevations (e.g., M3, M6) compared to lower elevations (e.g., ZAC), which results in shallower (steeper) STG in response to the positive (negative) anomaly of Z500 and P_{surf} over the ZR (Fig. 12). In particular, subsidence of air in a high-pressure system can cause cold and dry air to drain along the valley slopes, and hence, favor the development of inversions. We find that inversion frequency and strength can be related to large-scale atmospheric conditions.

The variability in the export of sea ice through the Fram Strait and in the GrSea has a regional-scale influence on the atmospheric condition along the east coast of Greenland (Hansen et al., 2008). In recent years, declining sea ice enhances heat and moisture transfer between the ocean and the atmosphere, resulting in an amplified Arctic warming (Serreze et al., 2009; Screen and Simmonds, 2010). We show that the atmospheric conditions in the GrSea and locally in the ZR, such as P_{surf}, T_{2m}, U, CCF, and precipitation, are influenced by SIF conditions. A comparison between the zonally averaged SIF over the GrSea and T_{2m} and precipitation in the ZR indicates that seasons with a SIF below (above) the reference period (1996–2020) are warmer (colder) and wetter (drier) than the average. Additionally, an increase (decrease) in q_{2m}, CCF, and U is associated with low (high) SIF days. These results are in line with other studies that show a strong linkage between sea-ice reduction and atmospheric warming in surrounding areas (Bhatt et al., 2010; Comiso, 2002; Hanna et al., 2004; Serreze et al., 2011; Stroeve et al., 2017), and increasing U, tropospheric moisture, CCF, and precipitation in the Arctic Seas (Stroeve et al., 2011; Müller et al., 2021; Deser et al., 2000; Francis et al., 2009; Jakobson et al., 2019; Overland and Wang, 2010; Schweiger et al., 2008; Alley et al., 2006; Schuster et al., 2021).

The STG in the ZR and changes in the SIF in the GrSea are correlated. The atmospheric response to the sea-ice variability can explain large parts of the observed STG variability in the ZR. Low P_{surf}, high U and q_{2m}, and large snowfall are associated with low SIF anomalies, thus favoring the formation of steep STG. Hinkler (2005) showed that the reductions in SIF lead to an increase in snowfall, which is in line with our result. Rogers et al. (2005) demonstrated that in mild winters with little sea-ice export through the Fram Strait, stronger and more frequent cyclones pass Northeast Greenland towards the Fram Strait. In contrast, during cold winters with high sea-ice export, cyclonic activity is more prevalent towards the Barents Sea and Eurasia side of the Arctic Ocean. Müller et al. (2021) found the linkage between the likelihood of occurrence of

extreme precipitation over Northwest Svalbard and the reducing sea-ice extent east of Greenland. The atmospheric
660   conditions such as high U, increase CCF accompanying cyclone and precipitation events decrease the stability of the
atmosphere, and hence steepen the STG.

Changes in the SIF could influence the SMB of the GrIS by the change in the near-surface air temperature and moisture
(Noël et al., 2014; Overland et al., 2012). The changes in sea ice may also affect the atmospheric conditions above
Greenland, thereby affecting the general circulation (Cho et al., 2022). Noël et al. (2014) found that GrIS SMB is insensitive
665   to changes in oceanic forcing because the katabatic winds flowing down the GrIS prevent the oceanic near-surface air from
entering inland. In contrast, Stroeve et al. (2017) found a correlation between the timing of melt onset over sea ice within the
Baffin Bay and the Davis Strait, and at the GrIS. They showed that an increase in the transfer of turbulent heat fluxes from
the ocean to the atmosphere during years with early sea-ice melt leads to higher air temperatures, humidity, and melt over the
GrIS. Furthermore, the increase in atmospheric moisture during low sea-ice conditions can also increase surface melt
670   through increased LWR_{in} (Bennartz et al., 2013; Van Tricht et al., 2016).

The negative SMB anomaly of the APO during the low SIF days is in line with the findings of Stroeve et al., (2017). As
a result of reduced sea ice, onshore winds might bring higher temperatures and moisture to the lower part of the APO, which
in turn could make the STG more negative (e.g., the average $STG_{AP2-AP1}$ anomaly is -1.5 ºC km^{-1} for ~17 SIF reduction,
implying AP1 is warmer than AP2), (Table S5) and increases surface melting there. However, unlike Stroeve et al. (2017)
675   we did not account for the time lag effect of the heat transfer from reduced sea-ice areas further inland to the GrIS. This
might have an effect on the magnitude of the SMB anomaly. Furthermore, the katabatic forcing of the APO could reduce the
impact of the near-surface air influenced by the ocean on the glacier boundary layer.

In Northeast Greenland's peripheral glaciers, Khan et al. (2022) observed a recent (October 2018–December 2021)
increase in snowfall at high altitudes partially offset the recent increase in the melt at low elevations. According to them, the
680   glacier plateau's high elevation (2000–3000 m) likely plays a crucial role in maintaining a viable accumulation area. This is
consistent with our observed contrasting signals of the summer SMB anomaly of the APO in the accumulation and ablation
areas, especially during low SIF days. Thus, in addition to plateau geometry, decreasing SIF likely leads to the observed
contrasting patterns in the accumulation and ablation area of Northeast Greenland's peripheral glaciers, especially during the
period 2018–2020 as shown by Khan et al. (2022), (Fig. S4).

685   **5   Conclusion**

The spatiotemporal variability of temperature gradients in orographically complex terrain, such as ZR, has been left
unexplored despite the sensitivity of Northeast Greenland's climate to climate change. To close this gap, this study
investigated the local climate variability, in particular T_{2m}, using the dense network of AWSs and combining data from
atmospheric reanalysis (ERA5) and a regional climate model (RACMO). More specifically, this study documented an

690   association between the STG, SIF, and other atmospheric variables in and around the ZR. In addition, we discuss the implications for the SMB of a local ice cap (APO). The main findings are as follows:

- The surface type and fjord-ice conditions are the dominating drivers governing the temporal evolution of the near-surface temperature distribution in the ZR. The presence of snow in the valley and an ice-covered fjord is favorable for the formation of shallow STG, possibly inversions. Whereas the snow-free valley and ice-free fjord favor the

695   steep STG. Moreover, the anomaly related to fjord-ice largely dominates within the surface layer close to ZAC.

- The STG within the ZR is strongly affected by the prevailing atmospheric pressure patterns; shallower (steeper) STGs are associated with a positive (negative) anomaly in Z500 and P_{surf} over eastern Greenland. This indicates when the upper air (~5500 m) is warmer (colder) than the mean atmospheric state, the STG within the valley is shallower (steeper). The patterns of these changes are consistent when different station pairs were employed.

700

- The change in the SIF has a similar impact on the terrestrial climate of the ZR and the climate over the GrSea. During high (low) SIF days over the GrSea, the STG in the ZR is shallower (steeper) than the mean value, e.g., the mean STG_{M3-ZAC} varies by ~4 ºC km^{-1} for a corresponding ~27 change in SIF over the GrSea. When SIF increases (decreases), the temperature at the bottom of the valley decreases (increases) more than at the top, resulting in a positive (negative) STG. Furthermore, the atmospheric response to the sea-ice variability can explain large parts of

705   the observed STG variability in the ZR. Low P_{surf}, high U, q_{2m}, and large snowfall are associated with low SIF anomalies, thus favoring the formation of steep STG.

- The change in SIF also shows an association with SMB change. For all seasons except for summer, the SMB anomaly of the APO is negative (positive) on high (low) SIF days which can be attributed to less (more) snowfall. However, the summer SMB anomaly shows a different pattern in the ablation and accumulation area of the APO.

710   During summer, days with high SIF are associated with a positive SMB anomaly in the ablation area (~16 mm w.e. day^{-1}) and a negative anomaly in the accumulation area (~-0.3 mm w.e. day^{-1}), indicating both less melt in the ablation area and less accumulation in the accumulation area. The decrease in T_{2m} and snowfall related to high SIF days can explain this opposite pattern in the ablation and accumulation area.

    The derived data from this study have significant implications for glacio-hydrological modeling by using the longest

715 temperature record available at the lowest elevation to simulate the historical temperature of the glacier. Additionally, the information on the magnitude and extent of local-scale processes is imperative for an efficient evaluation of regional as well as global climate models. The surface-atmosphere linkages described in this study would also be relevant in other parts of Greenland with a similar topographic setting (e.g., using AWSs from DMI). As a result, having this assurance can give us a better perspective on this unresolved matter and add confidence to the universality of the existing relationship. Besides, this

720 study highlights the complexity of the intertwined processes like sea-ice variability and terrestrial temperature gradient, and set the stage for more detailed process-oriented studies about the effects of climate change on a high arctic ecosystem.

Data availability. Derived data supporting the finding of this study are available from the corresponding author on request.

Author Contributions. SS, JA, and WS contributed to the study conception and design. SS downloaded and analyzed the data. The first draft of the manuscript was written by SS and all authors discussed the results and contributed to the final manuscript.

Competing interest. The authors declare no conflict of interest.

Funding. Article processing charge is provided by the University of Graz.

Acknowledgments. We acknowledge the financial support for article publication by the University of Graz. We sincerely thank all providers of data. The UAV data was provided by the University of Graz. ERA5 data were supported by European Centre for Medium Weather Forecasting (ECMWF). Observational data from the Greenland Ecosystem Monitoring Programme were provided by Department of Bioscience, Aarhus University (Denmark), Department of Geosciences and Natural Resource Management, Copenhagen University (Denmark), Asiaq–Greenland Survey (Greenland), Geological Survey of Denmark and Greenland (GEUS) (Denmark), and Greenland Institute of Natural Resources (Greenland). We are grateful to Brice Noël for his help in providing the Regional Atmospheric Climate Model (RACMO) dataset and related detailed information.

6   References

Abermann, J., Hansen, B., Lund, M., Wacker, S., Karami, M., and Cappelen, J.: Hotspots and key periods of Greenland climate change during the past six decades, Ambio, 46, 3–11, https://doi.org/10.1007/s13280-016-0861-y, 2017.

Alley, R. B., Dupont, T. K., Parizek, B. R., Anandakrishnan, S., Lawson, D. E., Larson, G. J., and Evenson, E. B.: Outburst flooding and the initiation of ice-stream surges in response to climatic cooling: A hypothesis, Geomorphology, 75, 76–89, https://doi.org/10.1016/j.geomorph.2004.01.011, 2006.

Anderson, P. S.: A Method for Rescaling Humidity Sensors at Temperatures Well below Freezing, J. Atmos. Ocean. Technol.,   11,   1388–1391,   https://doi.org/https://journals.ametsoc.org/view/journals/atot/11/5/1520-0426_1994_011_1388_amfrhs_2_0_co_2.xml, 1994.

Van As, D.: Warming, glacier melt and surface energy budget from weather station observations in the melville bay region of northwest greenland, J. Glaciol., 57, 208–220, https://doi.org/10.3189/002214311796405898, 2011.

Ayala, A., Pellicciotti, F., MacDonell, S., McPhee, J., Vivero, S., Campos, C., and Egli, P.: Modelling the hydrological response of debris-free and debris-covered glaciers to present climatic conditions in the semiarid Andes of central Chile, Hydrol. Process., 30, 4036–4058, https://doi.org/10.1002/hyp.10971, 2016.

Ballinger, T. J., Hanna, E., Hall, R. J., Cropper, T. E., Miller, J., Ribergaard, M. H., Overland, J. E., and Høyer, J. L.: Anomalous blocking over Greenland preceded the 2013 extreme early melt of local sea ice, Ann. Glaciol., 59, 181–190, https://doi.org/DOI: 10.1017/aog.2017.30, 2018a.

Ballinger, T. J., Hanna, E., Hall, R. J., Miller, J., Ribergaard, M. H., and Høyer, J. L.: Greenland coastal air temperatures linked to Baffin Bay and Greenland Sea ice conditions during autumn through regional blocking patterns, Clim. Dyn., 50,
755   83–100, https://doi.org/10.1007/s00382-017-3583-3, 2018b.

Bennartz, R., Shupe, M. D., Turner, D. D., Walden, V. P., Steffen, K., Cox, C. J., Kulie, M. S., Miller, N. B., and Pettersen, C.: July 2012 Greenland melt extent enhanced by low-level liquid clouds, Nature, 496, 83–86, https://doi.org/10.1038/nature12002, 2013.

Bhatt, U. S., Walker, D. A., Raynolds, M. K., Comiso, J. C., Epstein, H. E., Jia, G., Gens, R., Pinzon, J. E., Tucker, C. J.,
760   Tweedie, C. E., and Webber, P. J.: Circumpolar Arctic Tundra Vegetation Change Is Linked to Sea Ice Decline, Earth Interact., 14, 1–20, https://doi.org/10.1175/2010EI315.1, 2010.

Bintanja, R. and Van Der Linden, E. C.: The changing seasonal climate in the Arctic, Sci. Rep., 3, 1556, https://doi.org/10.1038/srep01556, 2013.

Bintanja, R. and Selten, F. M.: Future increases in Arctic precipitation linked to local evaporation and sea-ice retreat, Nature,
765   509, 479–482, https://doi.org/10.1038/nature13259, 2014.

de Boer, G., Houston, A., Jacob, J., Chilson, P. B., Smith, S. W., Argrow, B., Lawrence, D., Elston, J., Brus, D., Kemppinen, O., Klein, P., Lundquist, J. K., Waugh, S., Bailey, S. C. C., Frazier, A., Sama, M. P., Crick, C., Schmale III, D., Pinto, J., Pillar-Little, E. A., Natalie, V., and Jensen, A.: Data generated during the 2018 LAPSE-RATE campaign: an introduction and overview, Earth Syst. Sci. Data, 12, 3357–3366, https://doi.org/10.5194/essd-12-3357-2020, 2020.

770   C3S: European State of the Climate 2019, 2019.

Cappelen, J., Jørgensen, B. V., Laursen, E. V., Stannius, L. S., and Thomsen, R. S.: The Observed Climate of Greenland, 1958-99 - with Climatological Standard Normals, 1961-90, Danish Meteorological Institute, Technical Report, 1–152 pp., 2001.

Cho, H., Kug, J.-S., and Jun, S.-Y.: Influence of the recent winter Arctic sea ice loss in short-term simulations of a regional
775   atmospheric model, Sci. Rep., 12, 8901, https://doi.org/10.1038/s41598-022-12783-4, 2022.

Chutko, K. J. and Lamoureux, S. F.: The influence of low-level thermal inversions on estimated melt-season characteristics in the central Canadian Arctic, Int. J. Climatol., 29, 259–268, https://doi.org/10.1002/joc.1722, 2009.

Citterio, M., Sejr, M. K., Langen, P. L., Mottram, R. H., Abermann, J., Hillerup Larsen, S., Skov, K., and Lund, M.: Towards quantifying the glacial runoff signal in the freshwater input to Tyrolerfjord–Young Sound, NE Greenland, Ambio,
780   46, 146–159, https://doi.org/10.1007/s13280-016-0876-4, 2017.

Comiso, J. C.: Correlation and trend studies of the sea-ice cover and surface temperatures in the Arctic, Ann. Glaciol., 34, 420–428, https://doi.org/DOI: 10.3189/172756402781818067, 2002.

Cullen, R. M. and Marshall, S. J.: Mesoscale Temperature Patterns in the Rocky Mountains and Foothills Region of Southern Alberta, Atmosphere-Ocean, 49, 189–205, https://doi.org/10.1080/07055900.2011.592130, 2011.

785   Delhasse, A., Kittel, C., Amory, C., Hofer, S., van As, D., Fausto, R. S., and Fettweis, X.: Brief communication: Evaluation of the near-surface climate in ERA5 over the Greenland Ice Sheet, Cryosph., 14, 957–965, https://doi.org/10.5194/tc-14-957-

2020, 2020.

Deser, C., Walsh, J. E., and Timlin, M. S.: Arctic Sea Ice Variability in the Context of Recent Atmospheric Circulation Trends, J. Clim., 13, 617–633, https://doi.org/10.1175/1520-0442(2000)013<0617:ASIVIT>2.0.CO;2, 2000.

790 Ding, Q., Schweiger, A., L'Heureux, M., Battisti, D. S., Po-Chedley, S., Johnson, N. C., Blanchard-Wrigglesworth, E., Harnos, K., Zhang, Q., Eastman, R., and Steig, E. J.: Influence of high-latitude atmospheric circulation changes on summertime Arctic sea ice, Nat. Clim. Chang., 7, 289–295, https://doi.org/10.1038/nclimate3241, 2017.

Djoumna, G., Mernild, S. H., and Holland, D. M.: Meteorological Conditions and Cloud Effects on Surface Radiation Balance Near Helheim Glacier and Jakobshavn Isbræ (Greenland) Using Ground-Based Observations, 795 https://doi.org/10.3389/feart.2020.616105, 2021.

Elberling, B., Tamstorf, M. P., Michelsen, A., Arndal, M. F., Sigsgaard, C., Illeris, L., Bay, C., Hansen, B. U., Christensen, T. R., Hansen, E. S., Jakobsen, B. H., and Beyens, L. B. T.-A. in E. R.: Soil and Plant Community-Characteristics and Dynamics at Zackenberg, in: High-Arctic Ecosystem Dynamics in a Changing Climate, vol. 40, Academic Press, 223–248, https://doi.org/https://doi.org/10.1016/S0065-2504(07)00010-4, 2008.

800 Fausto, R. S., Van As, D., Mankoff, K. D., Vandecrux, B., Citterio, M., Ahlstrøm, A. P., Andersen, S. B., Colgan, W., Karlsson, N. B., Kjeldsen, K. K., Korsgaard, N. J., Larsen, S. H., Nielsen, S., Pedersen, A. Ø., Shields, C. L., Solgaard, A. M., and Box, J. E.: PROMICE automatic weather station data, Earth Syst. Sci. Data Discuss., 2021, 1–41, https://doi.org/10.5194/essd-2021-80, 2021.

Fettweis, X., Mabille, G., Erpicum, M., Nicolay, S., and den Broeke, M. Van: The 1958–2009 Greenland ice sheet surface 805 melt and the mid-tropospheric atmospheric circulation, Clim. Dyn., 36, 139–159, https://doi.org/10.1007/s00382-010-0772-8, 2011.

Fettweis, X., Hanna, E., Lang, C., Belleflamme, A., Erpicum, M., and Gallée, H.: *Brief communication* "Important role of the mid-tropospheric atmospheric circulation in the recent surface melt increase over the Greenland ice sheet," Cryosph., 7, 241–248, https://doi.org/10.5194/tc-7-241-2013, 2013.

810 Forbush, S. E., Pomerantz, M. A., Duggal, S. P., and Tsao, C. H.: Statistical considerations in the analysis of solar oscillation data by the superposed epoch method, Sol. Phys., 82, 113–122, https://doi.org/10.1007/BF00145551, 1983.

Francis, J. A., Chan, W., Leathers, D. J., Miller, J. R., and Veron, D. E.: Winter Northern Hemisphere weather patterns remember summer Arctic sea-ice extent, Geophys. Res. Lett., 36, https://doi.org/https://doi.org/10.1029/2009GL037274, 2009.

815 Gao, L., Bernhardt, M., and Schulz, K.: Elevation correction of ERA-Interim temperature data in complex terrain, Hydrol. Earth Syst. Sci, 16, 4661–4673, https://doi.org/10.5194/hess-16-4661-2012, 2012.

Gardner, A. S., Sharp, M. J., Koerner, R. M., Labine, C., Boon, S., Marshall, S. J., Burgess, D. O., and Lewis, D.: Near-surface temperature lapse rates over arctic glaciers and their implications for temperature downscaling, J. Clim., https://doi.org/10.1175/2009JCLI2845.1, 2009.

820 GEM: ClimateBasis Zackenberg - Air temperature - Air temperature, 200cm @ 60min sample (°C) (Version 1.0) [Data set],

https://doi.org/10.17897/XV96-HC57, 2020a.

GEM: GeoBasis Zackenberg - Meteorology - M2 (Version 1.0) [Data set], https://doi.org/10.17897/7WAM-6143, 2020b.

GEM: GeoBasis Zackenberg - Meteorology - M3 (Version 1.0) [Data set], https://doi.org/10.17897/7JXY-VX51, 2020c.

GEM: GeoBasis Zackenberg - Meteorology - M6_60min (Version 1.0) [Data set], https://doi.org/10.17897/SEFH-AM39,
825 2020d.

GEM: GeoBasis Zackenberg - Meteorology - M7 (Version 1.0) [Data set], https://doi.org/10.17897/D081-0X68, 2020e.

GEM: GeoBasis Zackenberg - Meteorology - M8 (Version 1.0) [Data set], https://doi.org/10.17897/1VH5-F517, 2020f.

GEM: GlacioBasis Zackenberg - Near surface weather - AWS-Zack-M (Version 1.0) [Data set],
https://doi.org/10.17897/KDSV-GH23, 2020g.

830 GEM: GlacioBasis Zackenberg - Near surface weather - AWS-Zack-S (Version 1.0) [Data set],
https://doi.org/10.17897/NVJ0-V931, 2020h.

GEM: GlacioBasis Zackenberg - Near surface weather - AWS-Zack-T (Version 1.0) [Data set],
https://doi.org/10.17897/3MD2-PZ63, 2020i.

GEM: MarineBasis Zackenberg - Sea ice conditions - Sea ice formation (Version 1.0) [Data set],
835 https://doi.org/10.17897/5MNP-KX83, 2020j.

Glickman, T. S.: Glossary of Meteorology, American Meteorological Society, 850, 2000.

Goff, J. A. and Gratch, S.: Low-pressure properties of water-from - 160 to 212° F, Trans. Am. Heat. Vent. Eng., 52, 95–121,
1946.

Graham, R. M., Hudson, S. R., and Maturilli, M.: Improved Performance of ERA5 in Arctic Gateway Relative to Four
840 Global Atmospheric Reanalyses, Geophys. Res. Lett., 46, 6138–6147, https://doi.org/10.1029/2019GL082781, 2019.

Hanna, E., Jónsson, T., and Box, J. E.: An analysis of Icelandic climate since the nineteenth century, Int. J. Climatol., 24,
1193–1210, https://doi.org/https://doi.org/10.1002/joc.1051, 2004.

Hanna, E., Mernild, S. H., Cappelen, J., and Steffen, K.: Recent warming in Greenland in a long-term instrumental (1881–
2012) climatic context: I. Evaluation of surface air temperature records, Environ. Res. Lett., 7, 45404,
845 https://doi.org/10.1088/1748-9326/7/4/045404, 2012.

Hanna, E., Fettweis, X., Mernild, S. H., Cappelen, J., Ribergaard, M. H., Shuman, C. A., Steffen, K., Wood, L., and Mote, T.
L.: Atmospheric and oceanic climate forcing of the exceptional Greenland ice sheet surface melt in summer 2012, Int. J.
Climatol., 34, 1022–1037, https://doi.org/https://doi.org/10.1002/joc.3743, 2014.

Hanna, E., Cropper, T. E., Jones, P. D., Scaife, A. A., and Allan, R.: Recent seasonal asymmetric changes in the NAO (a
850 marked summer decline and increased winter variability) and associated changes in the AO and Greenland Blocking Index,
Int. J. Climatol., 35, 2540–2554, https://doi.org/https://doi.org/10.1002/joc.4157, 2015.

Hanna, E., Cropper, T. E., Hall, R. J., and Cappelen, J.: Greenland Blocking Index 1851–2015: a regional climate change
signal, Int. J. Climatol., 36, 4847–4861, https://doi.org/https://doi.org/10.1002/joc.4673, 2016.

Hanna, E., Cappelen, J., Fettweis, X., Mernild, S. H., Mote, T. L., Mottram, R., Steffen, K., Ballinger, T. J., and Hall, R. J.:

855   Greenland surface air temperature changes from 1981 to 2019 and implications for ice-sheet melt and mass-balance change, Int. J. Climatol., 41, E1336–E1352, https://doi.org/https://doi.org/10.1002/joc.6771, 2021.

Hansen, B. U., Sigsgaard, C., Rasmussen, L., Cappelen, J., Hinkler, J., Mernild, S. H., Petersen, D., Tamstorf, M. P., Rasch, M., and Hasholt, B.: Present-Day Climate at Zackenberg, in: Advances in Ecological Research, vol. 40, Academic Press, 111–149, https://doi.org/10.1016/S0065-2504(07)00006-2, 2008.

860   Hemingway, B. L., Frazier, A. E., Elbing, B. R., and Jacob, J. D.: Vertical Sampling Scales for Atmospheric Boundary Layer Measurements from Small Unmanned Aircraft Systems (sUAS), https://doi.org/10.3390/atmos8090176, 2017.

Hersbach, H., Bell, B., Berrisford, P., Biavati, G., Horányi, A., Muñoz Sabater, J., Nicolas, J., Peubey, C., Radu, R., Rozum, I., Schepers, D., Simmons, A., Soci, C., Dee, D., and Thépaut, J.-N.: ERA5 hourly data on pressure levels from 1979 to present. Copernicus Climate Change Service (C3S) Climate Data Store (CDS), https://doi.org/10.24381/cds.bd0915c6, 865   2018a.

Hersbach, H., Bell, B., Berrisford, P., Biavati, G., Horányi, A., Muñoz Sabater, J., Nicolas, J., Peubey, C., Radu, R., Rozum, I., Schepers, D., Simmons, A., Soci, C., Dee, D., and Thépaut, J.-N.: ERA5 hourly data on single levels from 1979 to present. Copernicus Climate Change Service (C3S) Climate Data Store (CDS), https://doi.org/10.24381/cds.adbb2d47, 2018b.

870   Hersbach, H., Bell, B., Berrisford, P., Horányi, A., Sabater, J. M., Nicolas, J., Radu, R., Schepers, D., Simmons, A., Soci, C., and Dee, D.: Global reanalysis: goodbye ERA-Interim, hello ERA5, ECMWF Newsl., 159, 2019.

Hersbach, H., Bell, B., Berrisford, P., Hirahara, S., Horányi, A., Muñoz-Sabater, J., Nicolas, J., Peubey, C., Radu, R., Schepers, D., Simmons, A., Soci, C., Abdalla, S., Abellan, X., Balsamo, G., Bechtold, P., Biavati, G., Bidlot, J., Bonavita, M., De Chiara, G., Dahlgren, P., Dee, D., Diamantakis, M., Dragani, R., Flemming, J., Forbes, R., Fuentes, M., Geer, A., 875   Haimberger, L., Healy, S., Hogan, R. J., Hólm, E., Janisková, M., Keeley, S., Laloyaux, P., Lopez, P., Lupu, C., Radnoti, G., de Rosnay, P., Rozum, I., Vamborg, F., Villaume, S., and Thépaut, J. N.: The ERA5 global reanalysis, Q. J. R. Meteorol. Soc., 146, 1999–2049, https://doi.org/10.1002/qj.3803, 2020.

Heynen, M., Miles, E., Ragettli, S., Buri, P., Immerzeel, W. W., and Pellicciotti, F.: Air temperature variability in a high-elevation Himalayan catchment, Ann. Glaciol., 57, 212–222, https://doi.org/10.3189/2016AoG71A076, 2016.

880   Hinkler, J.: From digital cameras to large scale sea-ice dynamics. A snow–ecosystem perspective. PhD thesis, University of Copenhagen, 184 pp., 2005.

Hofer, S., Tedstone, A. J., Fettweis, X., and Bamber, J. L.: Decreasing cloud cover drives the recent mass loss on the Greenland Ice Sheet, Sci. Adv., 3, e1700584, https://doi.org/10.1126/sciadv.1700584, 2017.

Hulth, J., Rolstad, C., Trondsen, K., and Rødby, R. W.: Surface mass and energy balance of Sørbreen, Jan Mayen, 2008, 885   Ann. Glaciol., 51, 110–119, https://doi.org/10.3189/172756410791392754, 2010.

iMet-XQ2 Second-Generation Atmospheric Sensor for UAV Deployment: https://www.intermetsystems.com/ee/pdf/202021_iMet-XQ2_210415.pdf, last access: 10 August 2021.

Isaksen, K., Nordli, Ø., Ivanov, B., Køltzow, M. A. Ø., Aaboe, S., Gjelten, H. M., Mezghani, A., Eastwood, S., Førland, E.,

Benestad, R. E., Hanssen-Bauer, I., Brækkan, R., Sviashchennikov, P., Demin, V., Revina, A., and Karandasheva, T.:
890   Exceptional warming over the Barents area, Sci. Rep., 12, 9371, https://doi.org/10.1038/s41598-022-13568-5, 2022.

Jakobson, L., Vihma, T., and Jakobson, E.: Relationships between Sea Ice Concentration and Wind Speed over the Arctic Ocean during 1979–2015, J. Clim., 32, 7783–7796, https://doi.org/10.1175/JCLI-D-19-0271.1, 2019.

Jensen, L. M., Christensen, T. R., and Schmidt, N. M.: Zackenberg Ecological Research Operations. 19th Annual Report, 2013, 130 pp., 2014.

895   Jiang, S., Ye, A., and Xiao, C.: The temperature increase in Greenland has accelerated in the past five years, Glob. Planet. Change, 194, 103297, https://doi.org/https://doi.org/10.1016/j.gloplacha.2020.103297, 2020.

Khan, S. A., Colgan, W., Neumann, T. A., van den Broeke, M. R., Brunt, K. M., Noël, B., Bamber, J. L., Hassan, J., and Bjørk, A. A.: Accelerating Ice Loss From Peripheral Glaciers in North Greenland, Geophys. Res. Lett., 49, e2022GL098915, https://doi.org/https://doi.org/10.1029/2022GL098915, 2022.

900   Kimball, S. K., Montalvo, C. J., and Mulekar, M. S.: Assessing iMET-XQ Performance and Optimal Placement on a Small Off-the-Shelf, Rotary-Wing UAV, as a Function of Atmospheric Conditions, https://doi.org/10.3390/atmos11060660, 2020.

Kirchner, M., Faus-Kessler, T., Jakobi, G., Leuchner, M., Ries, L., Scheel, H.-E., and Suppan, P.: Altitudinal temperature lapse rates in an Alpine valley: trends and the influence of season and weather patterns, Int. J. Climatol., 33, 539–555, https://doi.org/https://doi.org/10.1002/joc.3444, 2013.

905   Laken, B. A. and Čalogović, J.: Composite analysis with Monte Carlo methods: an example with cosmic rays and clouds, J. Sp. Weather Sp. Clim., 3, 2013.

Marshall, S. J., Sharp, M. J., Burgess, D. O., and Anslow, F. S.: Near-surface-temperature lapse rates on the Prince of Wales Icefield, Ellesmere Island, Canada: implications for regional downscaling of temperature, Int. J. Climatol., 27, 385–398, https://doi.org/https://doi.org/10.1002/joc.1396, 2007.

910   Van Meijgaard, E., van Ulft, L. H., Van de Berg, W. J., Bosveld, F. C., van den Hurk, B. J. J. M., Lenderink, G., and Siebesma, A. P.: The KNMI regional atmospheric climate model RACMO version 2.1, Tech. Rep. 302, 2008.

Meltofte, H. and Rasch, M.: The Study Area at Zackenberg, in: Advances in Ecological Research, vol. 40, Academic Press, 101–110, https://doi.org/10.1016/S0065-2504(07)00005-0, 2008.

Meltofte, H. and Thing, H.: Zackenberg Ecological Research Operations, 1st Annual Report, 1995.— Danish Polar Center,
915   Ministry of Research & Technology, 1996.

Mernild, S. H. and Liston, G. E.: The Influence of air temperature inversions on snowmelt and glacier mass balance simulations, Ammassalik Island, Southeast Greenland, J. Appl. Meteorol. Climatol., https://doi.org/10.1175/2009JAMC2065.1, 2010.

Mernild, S. H., Hasholt, B., and Liston, G. E.: Climatic control on river discharge simulations, Zackenberg River drainage
920   basin, northeast Greenland, Hydrol. Process., 22, 1932–1948, https://doi.org/https://doi.org/10.1002/hyp.6777, 2008.

Mernild, S. H., Hanna, E., Yde, J. C., Cappelen, J., and Malmros, J. K.: Coastal Greenland air temperature extremes and trends 1890–2010: annual and monthly analysis, Int. J. Climatol., 34, 1472–1487, https://doi.org/10.1002/joc.3777, 2014.

Minder, J. R., Mote, P. W., and Lundquist, J. D.: Surface temperature lapse rates over complex terrain: Lessons from the Cascade Mountains, J. Geophys. Res, 115, https://doi.org/10.1029/2009JD013493, 2010.

925 Müller, M., Kelder, T., and Palerme, C.: Decline of sea-ice in the Greenland Sea intensifies extreme precipitation over Svalbard, Weather Clim. Extrem., https://doi.org/10.31223/X56S53, 2021.

Nielsen-Englyst, P., Høyer, J. L., Madsen, K. S., Tonboe, R., Dybkjaer, G., and Alerskans, E.: In situ observed relationships between snow and ice surface skin temperatures and 2 m air temperatures in the Arctic, Cryosph., 13, 1005–1024, https://doi.org/10.5194/tc-13-1005-2019, 2019.

930 Noël, B., Fettweis, X., Van De Berg, W. J., van den Broeke, M. R., and Erpicum, M.: Sensitivity of Greenland Ice Sheet surface mass balance to perturbations in sea surface temperature and sea ice cover: a study with the regional climate model MAR, Cryosph., 8, 1871–1883, https://doi.org/10.5194/tc-8-1871-2014, 2014.

Noël, B., Van De Berg, W. J., Van Meijgaard, E., Kuipers Munneke, P., Van De Wal, R. S. W., and Van Den Broeke, M. R.: Evaluation of the updated regional climate model RACMO2.3: Summer snowfall impact on the Greenland Ice Sheet,
935 Cryosphere, 9, 1831–1844, https://doi.org/10.5194/TC-9-1831-2015, 2015.

Noël, B., van de Berg, W. J., Lhermitte, S., Wouters, B., Machguth, H., Howat, I., Citterio, M., Moholdt, G., Lenaerts, J. T. M., and van den Broeke, M. R.: A tipping point in refreezing accelerates mass loss of Greenland's glaciers and ice caps, Nat. Commun., 8, 14730, https://doi.org/10.1038/ncomms14730, 2017.

Noël, B., van de Berg, W. J., van Wessem, J. M., van Meijgaard, E., van As, D., Lenaerts, J. T. M., Lhermitte, S., Kuipers
940 Munneke, P., Smeets, C. J. P. P., van Ulft, L. H., van de Wal, R. S. W., and van den Broeke, M. R.: Modelling the climate and surface mass balance of polar ice sheets using RACMO2 – Part 1: Greenland (1958–2016), Cryosph., 12, 811–831, https://doi.org/10.5194/tc-12-811-2018, 2018.

Noël, B., Van De Berg, W. J., Lhermitte, S., and van den Broeke, M. R.: Rapid ablation zone expansion amplifies north Greenland mass loss, Sci. Adv., 5, 1–9, https://doi.org/10.1126/sciadv.aaw0123, 2019.

945 Ohmura, A.: Earth's Surface Energy Balance, https://doi.org/https://doi.org/10.1002/9781119300762.wsts0127, 29 December 2019.

Olesen, J. M., Dupont, Y. L., O'Gorman, E., Ings, T. C., Layer, K., Melián, C. J., Trøjelsgaard, K., Pichler, D. E., Rasmussen, C., and Woodward, G.: Chapter 1 - From Broadstone to Zackenberg: Space, Time and Hierarchies in Ecological Networks, in: Ecological Networks, vol. 42, edited by: Woodward, G. B. T.-A. in E. R., Academic Press, 1–69,
950 https://doi.org/https://doi.org/10.1016/B978-0-12-381363-3.00001-0, 2010.

Ono, J., Watanabe, M., Komuro, Y., Tatebe, H., and Abe, M.: Enhanced Arctic warming amplification revealed in a low-emission scenario, Commun. Earth Environ., 3, 27, https://doi.org/10.1038/s43247-022-00354-4, 2022.

Overland, J. E. and Wang, M.: Large-scale atmospheric circulation changes are associated with the recent loss of Arctic sea ice, Tellus A Dyn. Meteorol. Oceanogr., 62, 1–9, https://doi.org/10.1111/j.1600-0870.2009.00421.x, 2010.

955 Overland, J. E., Francis, J. A., Hanna, E., and Wang, M.: The recent shift in early summer Arctic atmospheric circulation, Geophys. Res. Lett., 39, https://doi.org/https://doi.org/10.1029/2012GL053268, 2012.

Pepin, N.: Lapse rate changes in northern England, Theor. Appl. Climatol., 68, 1–16, https://doi.org/10.1007/s007040170049, 2001.

Pepin, N. and Losleben, M.: Climate change in the Colorado Rocky Mountains: free air versus surface temperature trends, Int. J. Climatol., 22, 311–329, https://doi.org/https://doi.org/10.1002/joc.740, 2002.

Pepin, N. C. and Seidel, D. J.: A global comparison of surface and free-air temperatures at high elevations, J. Geophys. Res. Atmos., 110, https://doi.org/https://doi.org/10.1029/2004JD005047, 2005.

Pepin, N. C., Arnone, E., Gobiet, A., Haslinger, K., Kotlarski, S., Notarnicola, C., Palazzi, E., Seibert, P., Serafin, S., Schöner, W., Terzago, S., Thornton, J. M., Vuille, M., and Adler, C.: Climate Changes and Their Elevational Patterns in the Mountains of the World, Rev. Geophys., 60, e2020RG000730, https://doi.org/https://doi.org/10.1029/2020RG000730, 2022.

Preece, J. R., Wachowicz, L. J., Mote, T. L., Tedesco, M., and Fettweis, X.: Summer Greenland Blocking Diversity and Its Impact on the Surface Mass Balance of the Greenland Ice Sheet, J. Geophys. Res. Atmos., 127, e2021JD035489, https://doi.org/https://doi.org/10.1029/2021JD035489, 2022.

Rogers, J. C., Yang, L., and Li, L.: The role of Fram Strait winter cyclones on sea ice flux and on Spitsbergen air temperatures, Geophys. Res. Lett., 32, https://doi.org/https://doi.org/10.1029/2004GL022262, 2005.

Rolland, C.: Spatial and Seasonal Variations of Air Temperature Lapse Rates in Alpine Regions, J. Clim., 16, 1032–1046, https://doi.org/10.1175/1520-0442(2003)016<1032:SASVOA>2.0.CO;2, 2003.

Savitzky, A. and Golay, M. J. E.: Smoothing and Differentiation of Data by Simplified Least Squares Procedures., Anal. Chem., 36, 1627–1639, https://doi.org/10.1021/ac60214a047, 1964.

Schuster, L., Maussion, F., Langhamer, L., and Moseley, G. E.: Lagrangian detection of precipitation moisture sources for an arid region in northeast Greenland: relations to the North Atlantic Oscillation, sea ice cover, and temporal trends from 1979 to 2017, Weather Clim. Dynam., 2, 1–17, https://doi.org/10.5194/wcd-2-1-2021, 2021.

Schweiger, A. J., Lindsay, R. W., Vavrus, S., and Francis, J. A.: Relationships between Arctic sea ice and clouds during autumn, J. Clim., 21, 4799–4810, https://doi.org/10.1175/2008JCLI2156.1, 2008.

Screen, J. A. and Simmonds, I.: The central role of diminishing sea ice in recent Arctic temperature amplification, Nature, 464, 1334–1337, https://doi.org/10.1038/nature09051, 2010.

Serreze, M. C. and Barry, R. G.: The Arctic Climate System, 2nd ed., Cambridge University Press, Cambridge, https://doi.org/DOI: 10.1017/CBO9781139583817, 2014.

Serreze, M. C., Barrett, A. P., Stroeve, J. C., Kindig, D. N., and Holland, M. M.: The emergence of surface-based Arctic amplification, Cryosph., 3, 11–19, https://doi.org/10.5194/tc-3-11-2009, 2009.

Serreze, M. C., Barrett, A. P., and Cassano, J. J.: Circulation and surface controls on the lower tropospheric air temperature field of the Arctic, J. Geophys. Res. Atmos., 116, https://doi.org/https://doi.org/10.1029/2010JD015127, 2011.

Shahi, S., Abermann, J., Heinrich, G., Prinz, R., and Schöner, W.: Regional variability and trends of temperature inversions in Greenland, J. Clim., 33, https://doi.org/10.1175/JCLI-D-19-0962.1, 2020.

Shepherd, T. G.: Effects of a warming Arctic, Science (80-.)., 353, 989–990, https://doi.org/10.1126/science.aag2349, 2016.

Sirpa, H., B., R. P., and L., W. D.: Atmospheric Blocking and Atlantic Multidecadal Ocean Variability, Science (80-.)., 334, 655–659, https://doi.org/10.1126/science.1205683, 2011.

Stendel, M., Christensen, J. H., and Petersen, D.: Arctic Climate and Climate Change with a Focus on Greenland, in: Advances in Ecological Research, vol. 40, Elsevier, 13–43, https://doi.org/10.1016/S0065-2504(07)00002-5, 2008.

995 Stranne, C., Nilsson, J., Ulfsbo, A., O'Regan, M., Coxall, H. K., Meire, L., Muchowski, J., Mayer, L. A., Brüchert, V., Fredriksson, J., Thornton, B., Chawarski, J., West, G., Weidner, E., and Jakobsson, M.: The climate sensitivity of northern Greenland fjords is amplified through sea-ice damming, Commun. Earth Environ., 2, 70, https://doi.org/10.1038/s43247-021-00140-8, 2021.

Stroeve, J. C., Serreze, M. C., Barrett, A., and Kindig, D. N.: Attribution of recent changes in autumn cyclone associated
1000 precipitation in the Arctic, Tellus A Dyn. Meteorol. Oceanogr., 63, 653–663, https://doi.org/10.1111/j.1600-0870.2011.00515.x, 2011.

Stroeve, J. C., Markus, T., Boisvert, L., Miller, J., and Barrett, A.: Changes in Arctic melt season and implications for sea ice loss, Geophys. Res. Lett., 41, 1216–1225, https://doi.org/https://doi.org/10.1002/2013GL058951, 2014.

Stroeve, J. C., Mioduszewski, J. R., Rennermalm, A., Boisvert, L. N., Tedesco, M., and Robinson, D.: Investigating the
1005 local-scale influence of sea ice on Greenland surface melt, Cryosph., 11, 2363–2381, https://doi.org/10.5194/tc-11-2363-2017, 2017.

Swinbank, W. C.: Long-wave radiation from clear skies, Q. J. R. Meteorol. Soc., 89, 339–348, https://doi.org/https://doi.org/10.1002/qj.49708938105, 1963.

Thayyen, R. J. and Dimri, A. P.: Slope Environmental Lapse Rate (SELR) of Temperature in the Monsoon Regime of the
1010 Western Himalaya , https://www.frontiersin.org/article/10.3389/fenvs.2018.00042, 2018.

Van Tricht, K., Lhermitte, S., Lenaerts, J. T. M., Gorodetskaya, I. V., L'Ecuyer, T. S., Noël, B., van den Broeke, M. R., Turner, D. D., and van Lipzig, N. P. M.: Clouds enhance Greenland ice sheet meltwater runoff, Nat. Commun., 7, 10266, https://doi.org/10.1038/ncomms10266, 2016.